PCCP

PAPER

View Article Online
View Journal | View Issue

Cite this: *Phys. Chem. Chem. Phys.*, 2023, **25**, 22437

Pulsed-ramped-field-ionisation zero-kinetic-energy photoelectron spectroscopy of the metastable rare-gas atoms Ar, Kr and Xe

Holger Herburger,[a] Vincent Wirth,[a] Urs Hollenstein[a] and Frédéric Merkt *[abc]

Received 21st June 2023,
Accepted 24th July 2023

DOI: 10.1039/d3cp02881j

rsc.li/pccp

The photoionisation of the metastable rare-gas atoms Rg = Ar, Kr and Xe is investigated at the Rg^+ [...]$(ns)^2(np)^5\ ^2P_{3/2} \leftarrow$ Rg[...]$(ns)^2(np)^5((n+1)s)^1\ ^3P_2$ photoionisation threshold (n = 3, 4 and 5 for Ar, Kr and Xe) using the technique of pulsed-ramped-field-ionisation zero-kinetic-energy (PRFI-ZEKE) photoelectron spectroscopy. This technique, which monitors the field ionisation of high Rydberg states induced by a slowly growing electric-field ramp after a prepulse of opposite polarity, was recently introduced to record photoelectron spectra with high resolution and high sensitivity [Harper, Chen, Boyé-Péronne and Gans, *Phys. Chem. Chem. Phys.*, 2022, **117**, 9353]. A tunable UV laser system with a bandwidth of 30 MHz is used here to establish the factors determining the resolution and overall accuracy of this new method. In particular, the effects of stray electric fields, and of the magnitude of the prepulse and the field ramp on PRFI-ZEKE photoelectron spectra are studied by combining experiments with numerical simulations of the field-ionisation of high Rydberg states and of the electron flight times from the ionisation spot to the detector. A spectral resolution of 0.05 cm^{-1} is demonstrated in the photoelectron spectrum of metastable Ar.

1 Introduction

Pulsed-field-ionisation zero-kinetic-energy (PFI-ZEKE) photoelectron spectroscopy is a high-resolution form of photoelectron spectroscopy which relies on the delayed pulsed-field ionisation of Rydberg states of very large principal quantum numbers ($n \gg 100$) that are located below the ionisation thresholds of atoms and molecules.[1–4] These states form a pseudo-continuum of long-lived (lifetimes $\gg$1 μs) bound states. To record PFI-ZEKE photoelectron spectra, one scans the frequency of a narrow-band laser across the successive ionisation thresholds of atoms and molecules and monitors the current of electrons generated by pulsed-field ionisation as a function of the laser frequency. The high resolution of the method results from the selective field ionisation of narrow ranges of high Rydberg states. Electric-field pulse sequences have been developed that enable the recording of photoelectron spectra at a spectral resolution of better than 0.1 cm^{-1},[5,6] and the observation of the rotational structure in the spectra of diatomic molecules with small rotational constants[7–10] and of polyatomic molecules with up to about 10 atoms.[11–15]

At the high n values probed by PFI-ZEKE photoelectron spectroscopy, the pulsed-field-ionisation dynamics is diabatic or hydrogenic.[16,17] The Rydberg states in the presence of an electric field of strength F (called Rydberg-Stark states hereafter) are labelled with the three quantum numbers n, k and m. k is the difference between the two quantum numbers n_1 and n_2 that arise in the solution of the Schrödinger equation for the H atom in parabolic coordinates[18] and m is the magnetic quantum number. k takes on values ranging from $-(n-|m|-1)$ to $(n-|m|-1)$ in steps of 2. In the range of electric fields relevant for PFI-ZEKE photoelectron spectroscopy, the Stark effect is in good approximation linear and the Stark shifts are well described by $3a_0eknF/2$, where a_0 is the Bohr radius and e the elementary charge. The most selective field-ionisation pulse sequences exploit the inversion of the linear Stark shifts of high Rydberg states upon reversal of the polarity of the electric field in combination with the fact that blue-shifted Rydberg-Stark states ionise at higher field strengths than red-shifted ones.[5,6] The highest resolution so far, 0.055 cm^{-1},[6] was obtained using a pulsed electric-field sequence consisting of a positive electric-field pulse F_1 (called prepulse) followed by a sequence of negative electric-field pulses F_i, i = 2, 3,... of increasing strength, the first ones of which fulfil the condition $|F_i| < F_1$ (see Fig. 1(a)). The field-ionisation signals generated by these negative-field pulses originate from blue-shifted Rydberg-Stark states that are not field ionised by the prepulse and which are

[a] *Institute for Molecular Physical Science, ETH Zürich, 8093 Zürich, Switzerland. E-mail: frederic.merkt@phys.chem.ethz.ch*
[b] *Department of Physics, ETH Zürich, 8093 Zürich, Switzerland*
[c] *Quantum Center, ETH Zürich, 8093 Zürich, Switzerland*

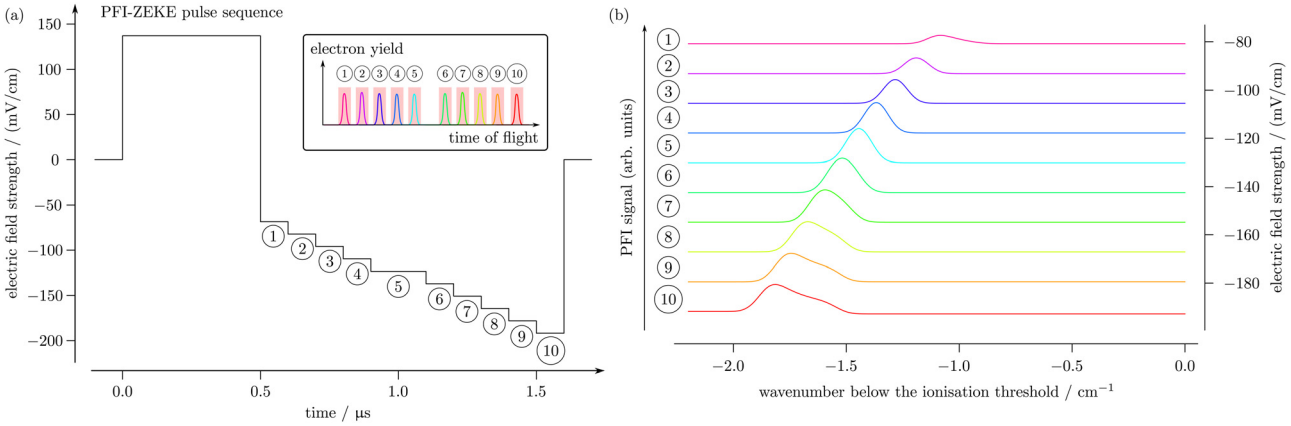

Fig. 1 (a) Electric-field pulse sequence used in high-resolution PFI-ZEKE photoelectron spectroscopy. Each of the field-ionisation pulses labelled 1–10 gives rise to a peak in the electron time-of-flight (TOF) spectra, as indicated schematically by the inset. (b) Calculated PFI-ZEKE photoelectron spectra corresponding to the different field pulses, as they would be observed by integrating the electron signal in the corresponding regions of the electron time-of-flight spectra and displaying the integrated signal as a function of the laser wavenumber.

converted into red-shifted Rydberg-Stark states when the polarity of the field inverses after the prepulse. The field-ionisation behaviour can be calculated using expressions for the ionisation rates of Rydberg-Stark states in electric fields derived by Damburg and Kolosov,[19] as previously demonstrated and explained in ref. 4, 6. In Fig. 1(a), the successive negative pulses giving rise to the photoelectron spectra are numbered from 1 to 10 and the time-of-flight distributions of the electrons generated by the successive pulses are schematically drawn in the inset. The spectral line shapes calculated for each of these pulses are compared in Fig. 1(b) and exhibit the following behaviour, already described in ref. 6: the lines corresponding to the successive pulses shift towards lower wavenumbers, reflecting the fact that the field required to ionise Rydberg states increases with decreasing n value. They are narrow for the first pulses (pulses 1–4), with a full width at half maximum (FWHM) of about 0.05 cm^{-1}, but gradually broaden and become asymmetric as soon as the field strength becomes larger than the field strength of the prepulse.

The resolution that can be achieved with pulse sequences of the type depicted in Fig. 1(a) improves if the electric-field step size is reduced but, at the same time, the signal and the signal-to-noise ratio of the PFI-ZEKE photoelectron spectra decrease. As long as the lines are symmetric and have approximately the same width, this problem can be overcome by shifting the spectra recorded for the different pulses along the wavenumber axis by the calculated field-induced shift and adding them up, as demonstrated, *e.g.*, in ref. 20–23.

Recently, Harper *et al.*[24] have investigated the limiting case of a field ramp, which corresponds to infinitesimal field increments between successive pulses and proposed an improved, more general and more flexible method to record high-resolution PFI-ZEKE photoelectron spectra. This method, called PRFI-ZEKE photoelectron spectroscopy for "pulsed-ramped-field-ionisation ZEKE photoelectron spectroscopy", replaces the sequence of negative-electric-field pulses of increasing strengths by a slowly growing negative-electric-field ramp, reminiscent of the very first ZEKE experiments by Reiser *et al.*[1] The ramp generates broad electron time-of-flight (TOF) distributions (see inset of Fig. 2(a)) instead of the discrete TOF peaks observed with sequences of discrete electric-field steps. The continuous distributions typically shift to shorter flight times at increasing wavenumbers, because Rydberg states of increasing n values ionise earlier in the ramp. Collecting the full electron time-of-flight distributions as a function of the laser wavenumber leads to two-dimensional spectra which

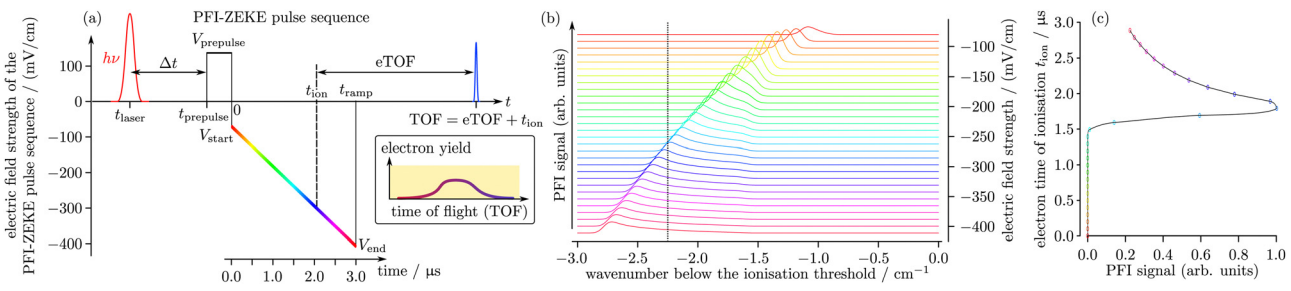

Fig. 2 (a) Slowly growing electric-field ramp as series of infinitesimally small field steps represented by the colour code. (b) Calculated PFI-ZEKE photoelectron spectra expected for the successive infinitesimal field steps, using the same colour code as in Panel (a). (c) Electron-TOF spectrum expected at the wavenumber marked by a dotted vertical line in Panel (b) and reconstructed by connecting, along this line, the signal strengths of the successive PFI-ZEKE photoelectron spectra and determining the time from the linear relationship between field strength and time during the ramp.

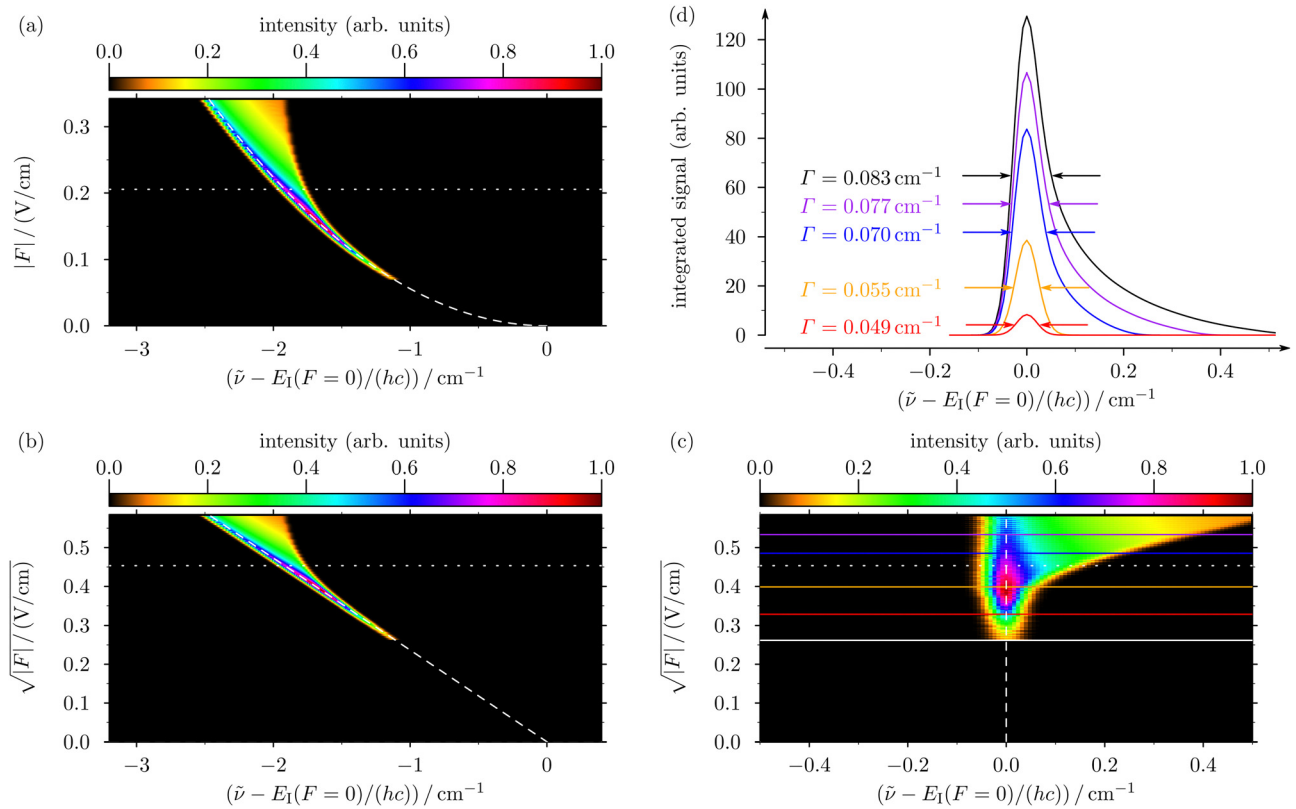

Fig. 3 (a) Numerical simulation of electron-time-of-flight spectra resulting from the field ionisation of high Rydberg states using a linear field ramp and assuming an idealised experimental configuration in which the electron flight times from the ionisation spot to the detector do not depend on the time and field at which the electrons are released during the ramp. The simulations were performed for a pulse sequence consisting of a prepulse of +0.21 V cm^{-1} followed by a negative-field ramp ranging from −0.07 to −0.34 V cm^{-1}. The data are presented in a two-dimensional spectrum (heat map) after converting the time-of-flight axis into an electric-field axis $|F|$ using the fact that the field is exactly proportional to the time during the field ramp. (b) Linearisation of Panel (a) by displaying the data as a function of $\sqrt{|F|}$. (c) Two-dimensional spectrum obtained after correction of the field-induced shift of the two-dimensional spectrum in Panel (b). In Panels (a)–(c), the dashed white lines indicate the extrapolation to the field-free threshold and the dotted white horizontal line marks the field strength of the prepulse. (d) One-dimensional photoelectron spectra obtained after integrating the field-corrected two-dimensional spectra along the vertical axis over the regions extending from the white horizontal line to the horizontal lines of the corresponding colours in Panel (c).

encode the full field-ionisation dynamics (see Fig. 3 of ref. 24) and contain the information needed to accurately determine the positions of the ionisation thresholds. A similar approach, based on the recording of two-dimensional maps of the field-ionisation signal was also used by Deller *et al.*[25] to study the rotational autoionisation dynamics in Rydberg states of NO. PRFI-ZEKE photoelectron spectroscopy can also be regarded as an extension of slow-electron imaging spectroscopy[26–28] to the pseudo-continuum of high Rydberg states below the ionisation thresholds.

Fig. 2 illustrates the relation between PFI-ZEKE photoelectron spectra recorded for a slowly growing pulsed ramp decomposed into a sequence of pulses with vanishingly small potential steps and the electron TOF spectra obtained at the different laser wavenumbers. Panel (a) depicts the pulse sequence with colour-coded field strength during the ramp. The PFI-ZEKE photoelectron spectra calculated for the successive fields are displayed in Panel (b) and correspond to the spectra that would be obtained by monitoring the electron signal over a narrow integration window of the electron-time-of-flight spectrum. The data presented in Panel (b) is a two-dimensional representation in which the electron signal is plotted as a function of both the excitation wavenumber and the field (and thus the time) at which the electrons were released. Panel (c) displays the electron-time-of-flight spectrum expected at the wavenumber indicated by the vertical dotted line in Panel (b). The electron-time-of-flight spectrum can indeed be reconstructed by connecting the signal strength of the successive PFI-ZEKE photoelectron spectra in Panel (b) and determining the time from the linear relationship between field strength and time during the ramp. This reconstruction is only approximate and assumes that the electron flight times from the ionisation spot to the detector are the same regardless of the field strength at the time of ionisation. This assumption enables one to directly relate the observed time-of-flight distributions to the times (and the fields) at which the corresponding electrons were released by field ionisation.

Applying this method to the PRFI-ZEKE photoelectron spectra of CO_2 and NO, Harper *et al.* demonstrated that a transformation of the two-dimensional spectra can be used to correct

for the field-induced shift of the thresholds and convert the two-dimensional spectra into one-dimensional photoelectron spectra at a resolution limited by the laser bandwidth (0.1 cm^{-1} in their case) without loss of sensitivity.[24] The principle of this transformation can be understood by considering the numerical simulations of the field-ionisation dynamics depicted in Fig. 3. These simulations assume an idealised experimental configuration in which the electron flight times do not depend on the time and the electric field at which the electrons are produced during the ramp. In the simulations, we assumed a laser excitation bandwidth of 0.04 cm^{-1}, corresponding to the spectral separation of two adjacent members of a Rydberg series at $n \approx 175$, with binding energy of -3.5 cm^{-1}. In this way, the Rydberg series appears as a pseudo-continuum over the range of electron binding energies covered by Fig. 3. Using a narrower laser bandwidth in the numerical simulations would lead to a modulation of the intensity distributions corresponding to the resolved excitation of the Rydberg series.

Fig. 3(a) depicts a calculated two-dimensional heat map of the electron time-of-flight spectra obtained at different wavenumbers (indicated along the bottom horizontal axis) below the field-free ionisation threshold $E_I(F = 0)$. The data is represented as a function of the ionisation field strength during the ramp along the vertical axis instead of the ionisation time. This two-dimensional representation provides the electron TOF spectra along vertical lines and PFI-ZEKE photoelectron spectra along horizontal lines. The intensity scale is provided at the top. The positions of the maxima of the electron TOF spectra, indicated by the dashed white line, scale as the square root of the electric field strength F_z. Consequently, representing the same data, but with $\sqrt{F_z}$ as vertical axis, leads to a straight line which intercepts the horizontal axis at the position of the field-free threshold, as illustrated in Panel (b). All PFI-ZEKE photoelectron spectra can be aligned at the zero-field position by compensating for the shift of the ionisation thresholds, *i.e.*, by moving each spectrum so that the dashed white line is now a vertical line at the position of the field-free ionisation threshold, as shown in Panel (c). By integrating the aligned spectra along the vertical axis, Harper *et al.* showed how to obtain PFI-ZEKE photoelectron spectra that simultaneously have high resolution and a good signal-to-noise ratio.[24] Panel (d) shows the spectra one obtains by integrating the electron signal depicted in Panel (c) along the vertical axis between the white horizontal line and the red, orange, blue, violet and top horizontal lines. As expected, the resolution decreases and the integrated intensity increases when the integration range becomes larger. As soon as the integration range extends to field strengths that are larger than the field strength of the prepulse (marked in Panels (a)–(c) by a dotted white line), the line profiles in the photoelectron spectra become blue degraded. This behaviour can be understood by considering Fig. 1. The key advantage of PRFI-ZEKE photoelectron spectroscopy over PFI-ZEKE photoelectron spectroscopy using staircase pulses is that the optimal compromise between resolution and signal strength can be found after the two-dimensional spectra have been recorded by deciding over which range the electron signal is integrated. Harper *et al.* also pointed out, in their analysis of the PRFI-ZEKE photoelectron spectrum of NO, that their procedure is well suited to identify contributions of autoionisation resonances to the intensity distribution of the photoelectron spectra.[24]

The main goals of the investigation presented here were to assess the resolution limit of PRFI-ZEKE photoelectron spectroscopy and to quantify potential systematic uncertainties in the determination of the field-free ionisation energies. To reach these goals, we chose the following approach: firstly, the method was applied to atomic systems. We chose the metastable rare-gas atoms Rg = Ar, Kr and Xe and recorded the PRFI-ZEKE photoelectron spectra of the Rg^+ $[\ldots](ns)^2(np)^5$ $^2P_{3/2} \leftarrow Rg[\ldots](ns)^2(np)^5((n+1)s)^1$ $^3P_2$ photoionisation transitions (n = 3, 4 and 5 for Ar, Kr and Xe), which all lie in the UV around 300 nm. The advantage of these systems is that the ionisation energies of metastable Ar, Kr and Xe are accurately known[29] and represent ideal references with which to compare the field-free ionisation energies derived from the PRFI-ZEKE photoelectron spectra. Secondly, to make sure that the resolution of the observed PRFI-ZEKE photoelectron spectra is not limited by the laser bandwidth, we used a pulsed UV laser system producing near-Fourier-transform-limited laser pulses with a bandwidth of better than 30 MHz, *i.e.*, about 300 times narrower than the laser bandwidth used in the pioneering study of Harper *et al.*[24] Finally, we carefully calibrated the electron flight times by combining full simulations of the field-ionisation process and of the electron trajectories so as not to have to rely on the assumption that these flight times are independent of the field strength at which field ionisation takes place during the ramp.

The remainder of this article is structured as follows: Section 2 provides a brief description of the experimental setup and explains the procedure followed to record and analyse the PRFI-ZEKE photoelectron spectra of the metastable rare-gas atoms. Particular attention is placed on the calibration of the electron flight times and the resulting systematic uncertainties in the determination of the field-free ionisation thresholds. Section 3 presents the experimental results and their analysis. The resolution limit of PRFI-ZEKE photoelectron spectroscopy is discussed in Section 4 and the last section summarises the main conclusions of this investigation.

2 Experimental procedure and numerical simulations

2.1 Experimental setup and procedure

A schematic overview of the experimental setup is presented in Fig. 4. It consists of a narrow-band near-Fourier-transform-limited UV laser tunable from 30 000 to 34 000 cm^{-1}, which will be described in detail elsewhere.[30] UV-laser pulses with a narrow frequency bandwidth are generated by pulse amplification and subsequent nonlinear frequency up-conversion of a single-mode continuous-wave ring dye laser (Coherent, Autoscan) pumped by a Nd-doped yttrium *ortho*-vanadate ($Nd:YVO_4$) laser (Coherent Verdi G10). The amplification was carried out

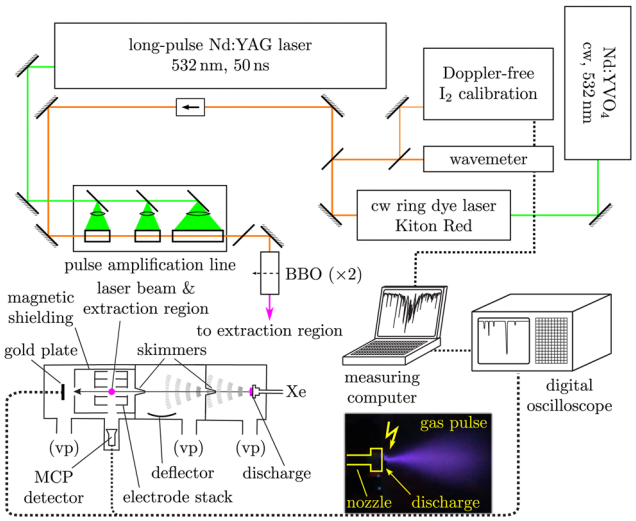

Fig. 4 Schematic representation of the experimental setup used to record PRFI-ZEKE photoelectron spectra of the metastable rare-gas atoms. The upper part of the figure shows the laser system including calibration, pulse-amplification, and frequency-upconversion devices. The lower part displays the experimental vacuum chambers (vp = vacuum pump) with supersonic beam, discharge source, photoexcitation and detection regions. See text for details.

using a pulsed-dye-amplification system (Radiant Dyes, NarrowAmp) with a range of dyes (Rhodamine 6G, Rhodamine B, or DCM) and pumped by the second-harmonic of a pulsed home-built Nd:YAG laser providing laser pulses with adjustable pulse durations up to ~2 μs. The Nd:YAG laser system was inspired by ref. 31–33. It consists of a linearly-polarised continuous-wave fibre laser (IPG Photonics, YLR-1-1064-LP-SF) operating at a wavelength of 1064 nm out of which laser pulses of adjustable duration in the range between 10 ns and 2 μs are chopped out using an amplitude modulator (JENOPTIK Optical Systems, AM1064b). The generated laser pulses are pulse-amplified in four Nd:YAG amplification stages (Northrop Grumman Cutting Edge Optronics, stage 1 and 2: RBAT34, stage 3: REA5006, stage 4: REA8006), out of which the first three stages are used in a double-pass configuration. Pulse energies up to 680 mJ per pulse are obtained. This radiation is frequency doubled in a 5 cm-long lithium-triborate (LBO, LiB_3O_5) crystal (Altechna) yielding pulse energies up to 120 mJ per pulse at 532 nm. In the experiments presented in this article, the dye-amplification chain was pumped using pulse energies of 30 mJ per pulse and pulse length of 50 ns. The pulse-amplified output of the dye-amplification chain, with fundamental wavenumber in the visible range between 15 000 and 17 000 cm^{-1}, was frequency doubled to the UV range between 30 000 and 34 000 cm^{-1} using a β-barium-borate (BBO, BaB_2O_4) crystal. The UV laser was operated at a repetition rate of 25 Hz, pulse energies of 200 μJ, a pulse length of 30 ns, and a bandwidth of 30 MHz, as measured by Doppler-free two-photon spectroscopy of atomic transitions.[30] The frequency of the pulse-amplified fundamental output of the laser was calibrated using a commercial wavemeter with a specified precision of 60 MHz (HighFinesse WS-7) and by recording Doppler-free spectra of I_2 for the absolute frequency calibration.[34]

The UV laser beam was directed into a high-vacuum photoexcitation chamber where it crossed a doubly skimmed supersonic beam containing the metastable rare-gas atoms at right angles in the arrangement depicted in Fig. 4. The supersonic expansion was produced using a pulsed valve, which was developed in the group of S. Leutwyler at the University of Bern.[35] The metastable rare-gas atoms were generated near the valve orifice in a home-built dielectric-ring-barrier discharge induced by AC potentials of up to several kV. Two skimmers with orifice diameters of 20 mm and 3 mm located 10 cm and 40 cm downstream of the nozzle orifice, respectively, were used to reduce the transverse velocity of the atoms in the photoexcitation region. During operation of the pulsed valve, the background pressure in the photoexcitation region typically rose from about 10^{-7} to 5×10^{-7} mbar. The beam velocities were determined to be 550, 380, and 305 m s^{-1} for Ar, Kr and Xe, respectively, by monitoring the time needed for the metastable atoms to reach the photoexcitation spot from the valve orifice. The geometric constraints imposed by the second skimmer limited the corresponding Doppler widths (FWHM) at wavenumbers around 30 000 cm^{-1} to 16 MHz, 10 MHz, and 8 MHz, for Ar, Kr, and Xe, respectively.

The PRFI-ZEKE photoelectron spectra were recorded by monitoring the field-ionisation signal induced by the electric-field pulse sequence depicted in Fig. 2(a). This sequence, consisting of a 1 μs-long potential prepulse (V_{prep}) immediately followed by a potential ramp of opposite polarity and varying linearly from V_{start} to V_{end} in typically 5 μs, was produced using an arbitrary-waveform generator (Agilent 33250A) and applied across an impedance-matched cylindrically symmetric and 7.8 cm-long stack of six equidistant and resistively coupled parallel electrodes. The last electrode on the side of the microchannel-plate (MCP) detector was grounded. The axis of the electrode stack pointed in the direction perpendicular to both the gas and laser beams, and the field-ionisation sequence extracted the electrons towards the MCP detector located at the end of a short TOF tube. The relative timings of the valve opening, the laser pulse, and the field-ionisation pulse sequence were controlled by delay generators (Stanford Research Instruments, Model DR-535 and PulseBlaster, Spincore Technologies). The electrode stack and the TOF tube were surrounded by a double-layer mumetal magnetic shield.

During each laser scan, the full electron TOF distribution was recorded at each frequency step with a sampling rate of 500 Msample s^{-1} using a digital oscilloscope (Teledyne Lecroy HDO6054A). Simultaneously, the I_2 frequency-calibration signal, the wavemeter signal, and the relative UV laser intensity were also recorded and stored. For the analysis of the electron-time-of-flight spectra, it is useful to consider the time at which the electrons reach the MCP detector as being the sum of the time (t_{ion}) at which the electron is produced by field ionisation during the field ramp and the actual time of flight of the electron (eTOF) from the ionisation spot to the detector (see Fig. 2(a)). Calibration of the electron TOF enables one to

determine the time of field ionisation and the corresponding value of the electric field, indicated by the vertical dashed line in Fig. 2(a).

2.2 Calibration of the electron times of flight and numerical simulations

To calibrate the electron times of flight, the electric-field distribution along the axis of the cylindrically symmetric electrode stack and adjacent TOF tube was calculated using the finite-element software SIMION (version 8.1)[36] for the sets of electric potentials applied in the experiments. As illustration, the electric-field distributions obtained when electric-potential differences of up to 10 V are applied across the electrode stack are depicted in Fig. 5. These distributions were used as input for the integration of Newton's equations of motion for the electrons using the initial conditions $v(t_{ion}) = 0$.

The calibration was performed by comparison with electron times of flight measured with electric-field pulse sequences such as that depicted in Fig. 6(a), which lead to discrete peaks in the electron TOF spectrum, as illustrated schematically in the inset of Fig. 1(a). The irregular time intervals between the different electric-potential steps in the sequence allowed us to unambiguously assign the different electron TOF peaks to the corresponding steps, as previously exploited by Dietrich *et al.*[37] The measured electron times of flight (black, with horizontal error bars) are compared in Fig. 6(c) with the times of flight predicted in the numerical simulations (blue curve) and to the

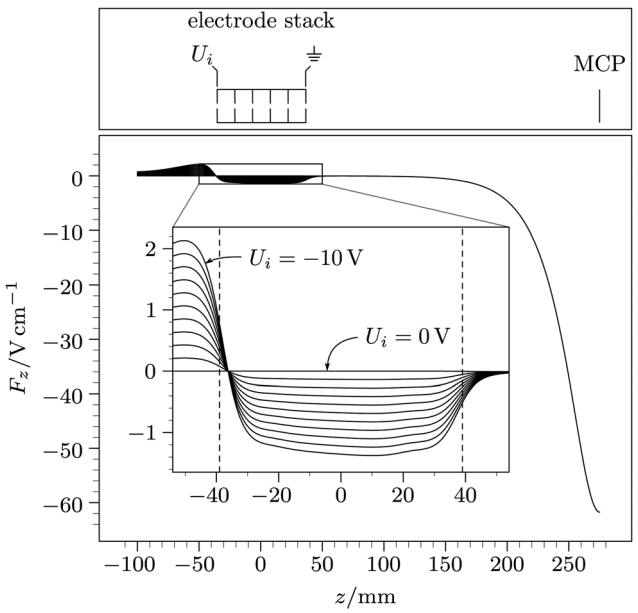

Fig. 5 Electric-field distribution along the axis of the electrode stack and adjacent TOF tube for a series of potentials U_i applied across the electrode stack ranging from 0 to −10 V in steps of −1 V. The positions z = 0, −39 mm and +39 mm correspond to the photoexcitation spot, the electron repeller plate and the grounded extraction plate at the entrance of the TOF tube, respectively. The large field increase beyond z = 150 mm results from the 221 V potential applied to the front plate of the MCP. The inset presents the electric-field distribution within the electrode stack on an enlarged scale.

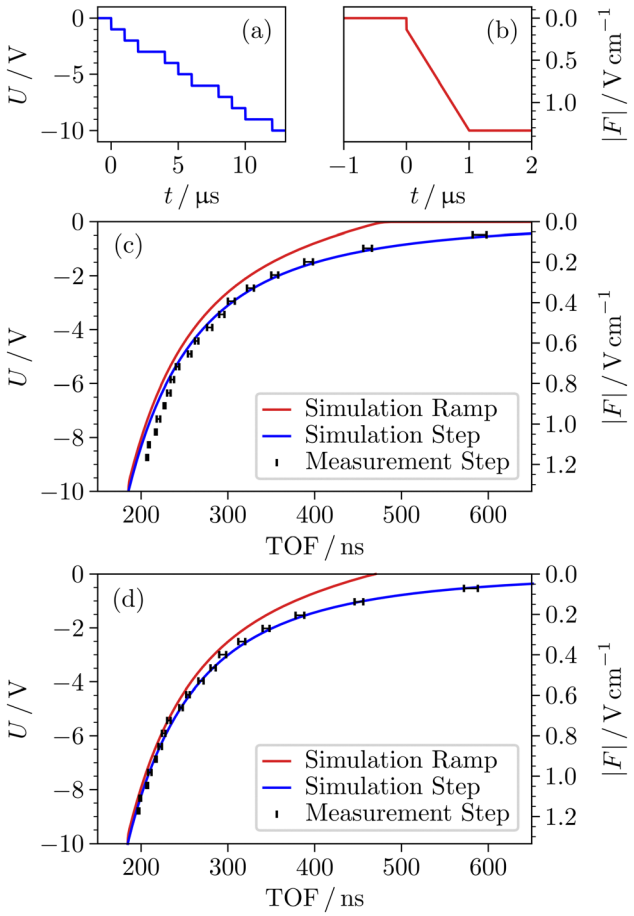

Fig. 6 (a) Sequence of electric-potential pulses used to calibrate the electron times of flight. (b) Typical ramped electric potential used to record the PRFI-ZEKE photoelectron spectra. (c) Comparison of electron times of flights measured using pulse sequences of the type depicted in Panel (a) (black, with horizontal error bars) with the corresponding calculated times of flight (blue curve). For comparison, the red curve shows the times of flight predicted for ramped potentials. (d) Same as Panel (c) but after introduction of an overall −10 ns shift of the time scale and a stray electric potential of −50 mV across the electrode stack.

times of flight predicted for the typical field ramp depicted in Fig. 6(b) (red curve). Significant deviations are only observed for the shortest times of flight and these could be eliminated by slight adjustments of the overall time scale (−10 ns) and by adding a weak stray potential of −50 mV across the stack, corresponding to a stray electric field of −6.4 mV cm^{-1} at the photoexcitation spot (see Fig. 6(d)). We attribute the time-scale correction to the different cable lengths used in the detection circuits and the finite response times of the amplifiers. Stray electric fields of several mV cm^{-1} are typical for the extraction stacks used in this work (see, *e.g.*, ref. 38).

The excellent agreement between measured and calculated electron times of flight over the entire range of electron–extraction potentials used in this work justifies the use of the calculated times of flight to determine accurate values of the electric field at the times of ionisation following the procedure outlined in Fig. 2. These electric-field values are, in turn, crucial

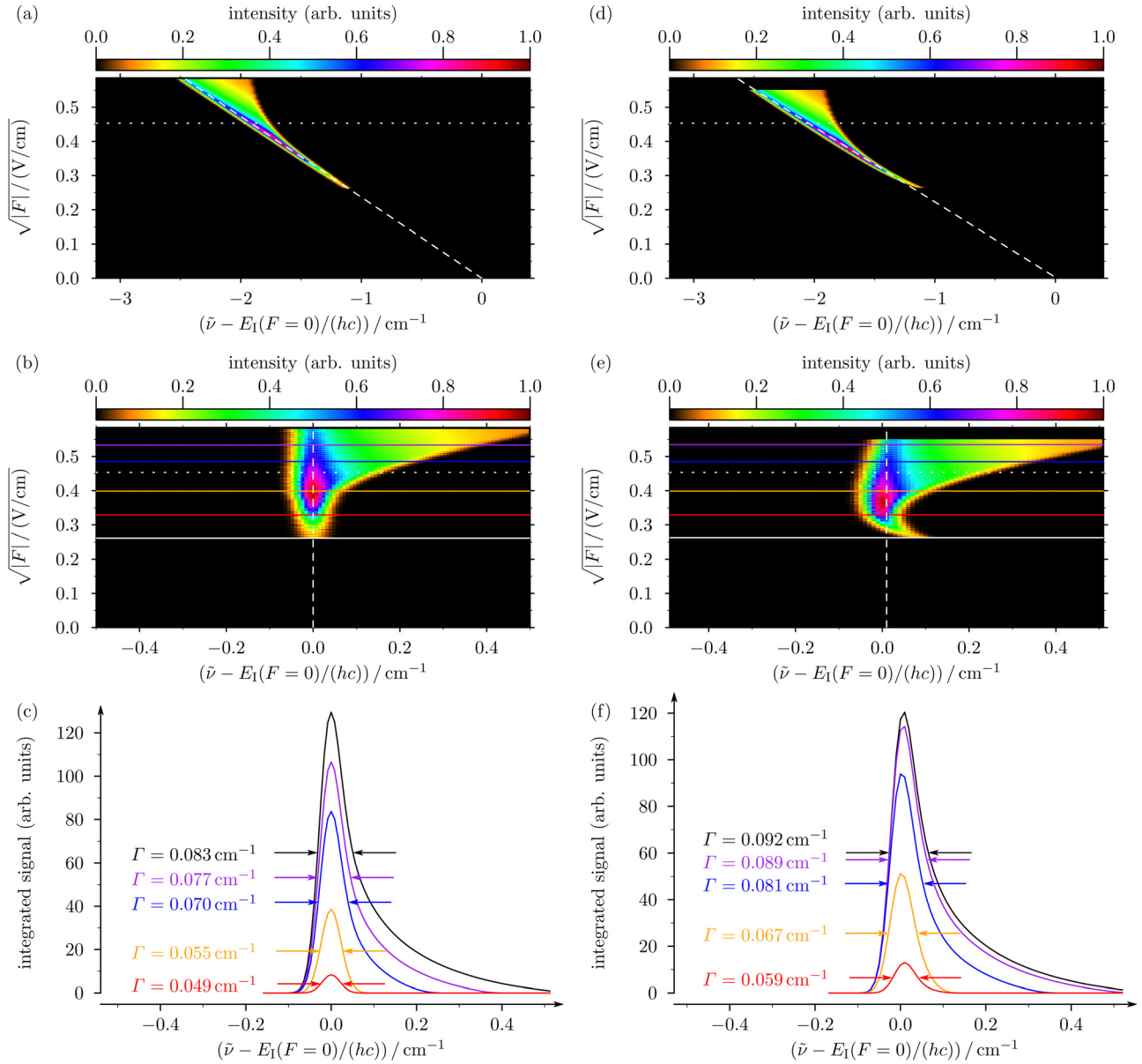

Fig. 7 Numerical simulation of the effect of the field dependence of the electron flight times on the resolution of PRFI-ZEKE photoelectron spectra and on the determination of the field-free ionisation energies. The simulations were performed for a pulse sequence consisting of a prepulse of +0.21 V cm^{-1} followed by a negative-field ramp ranging from −0.07 to −0.34 V cm^{-1}. (a)–(c): PRFI-ZEKE photoelectron spectra obtained when considering the fact that the electron flight times depend on the electric field at which the electrons are generated during the electric-field ramp. These panels correspond to Panels (b)–(d) of Fig. 3 and the dashed white line indicates the extrapolation to the field-free threshold. The dotted white horizontal line marks the field strength of the prepulse. (d)–(f) Same as Panels (a)–(c), but assuming that the electron flight times are the same regardless of the field at which they were generated during the field ramp.

to reliably correct for the field-induced shifts of the ionisation thresholds.

The simulations in Fig. 7 compare the results one obtains assuming that all electron flight times are identical regardless of the ionisation time during the ramp to the results obtained if one considers the actual electron flight times as given by the red line in Fig. 6. The left panels (Panels (a)–(c)) were obtained by considering the actual electron flight times to determine the field-ionisation time (t_{ion}) and the corresponding electric field. As expected, the results presented in these three panels exactly match the results presented in Panels (b)–(d) of Fig. 3. The three right panels of the figure (Panels (d)–(f)) were obtained by neglecting the electric-field dependence of the electron flight times. Comparison with the results presented in Panels (a)–(c) reveals significant distortions of the two-dimensional spectra. The field dependence of the electron flight times is largest at low fields, *i.e.*, early in the ramp, and causes deviations of the positions of the intensity maxima of the TOF spectra from the white dashed straight line in Panel (d) at positions around 1 cm^{-1} below the field-free threshold. The deviations are

particularly noticeable after correction for the field-induced shift in Panel (e). The comparison of the calculated two-dimensional PRFI-ZEKE photoelectron spectra in Panels (c) and (f) demonstrates that disregarding the field-dependence of the flight times in our experimental geometry leads to a shift of the position of the extrapolated field-free ionisation threshold by about 0.1 cm^{-1} at the tip of the distribution on the low-field side of Fig. 7(e). Moreover, it also leads to a slight spectral broadening of the one-dimensional spectra obtained by integration along the vertical axis. The actual broadening is partly masked by the 0.04 cm^{-1} bandwidth chosen for the simulations to avoid intensity modulations from the excitation of discrete Rydberg states in the spectral range of interest. Whereas the line shifts and line broadening apparent in Fig. 7(f) are too small to have played a role at the spectral resolution of 0.2 cm^{-1} in the investigation of Harper *et al.*,[24] they must be considered if one is to establish the resolution limit of PRFI-ZEKE photoelectron spectroscopy in our experimental setup. The field-dependence of the electron flight times was therefore included in the analysis of all results presented in the next section.

3 Experimental results

3.1 Argon

Fig. 8 presents the PRFI-ZEKE photoelectron spectra of the $(3p)^5\ ^2P_{3/2} \leftarrow (3p)^5(4s)^1\ ^3P_2$ photoionisation transition of Ar recorded with a pulse sequence consisting of a prepulse of 0.21 V cm^{-1} followed by a negative-field ramp from −0.07 to −0.34 V cm^{-1}. The colours for the heat map and the spectral and electric-field ranges were chosen to facilitate the comparison with the numerical simulations presented in Fig. 7(a)–(c). To obtain the fields at the time of ionisation, the electron flight times determined from numerical particle-trajectory simulations were subtracted from the electron-detection times, as illustrated in Fig. 2(a). The two-dimensional spectrum shown in Panel (a) displays the measured electron signal as a function of the square root of the electric-field strength and the laser excitation wavenumber. The white dashed line corresponds to a linear regression through the maxima of the electron TOF spectra based on the equation

$$\frac{\tilde{\nu}}{\mathrm{cm}^{-1}} = \frac{E_\mathrm{I}}{hc\,\mathrm{cm}^{-1}} - c_\mathrm{F}\sqrt{\frac{F}{\mathrm{V\,cm}^{-1}}} \qquad (1)$$

and is used to determine the field-free ionisation threshold, as explained in the discussion of Fig. 3 and 7. The analysis yields a value $E_\mathrm{I}/(hc)$ = 33 966.07(4) cm^{-1} for the ionisation energy of the $(3p)^5(4s)^1\ ^3P_2$ metastable state of Ar and a slope corresponding to c_F = −3.3(4) in eqn (1) for the dashed line. The same data are depicted on an expanded wavenumber scale in Panel (b) after correction of the field-induced shifts of the ionisation threshold. In this panel, the position of the field-free ionisation threshold is indicated by the vertical dashed white line. The areas between the full white horizontal line and the coloured ones define the integration ranges used to obtain the one-dimensional PRFI-ZEKE photoelectron spectra depicted in Panel (c).

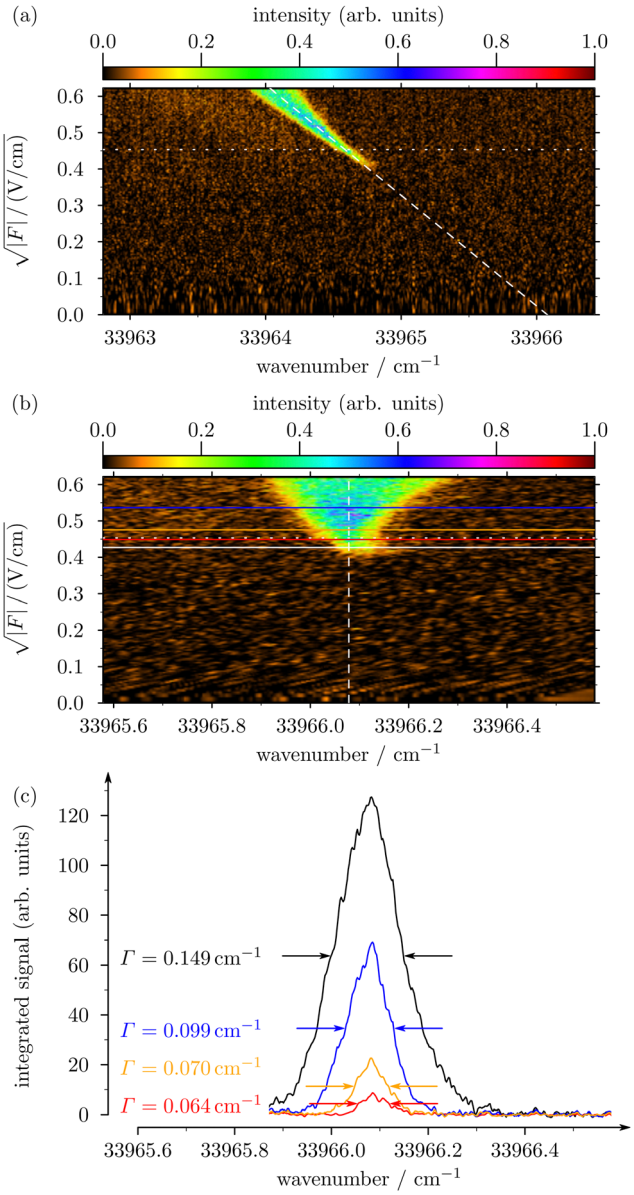

Fig. 8 PRFI-ZEKE photoelectron spectra of the $(3p)^5\ ^2P_{3/2} \leftarrow (3p)^5(4s)^1\ ^3P_2$ photoionisation transition of Ar recorded with a pulse sequence consisting of a prepulse of 0.21 V cm^{-1} followed by a negative-field ramp from −0.07 to −0.34 V cm^{-1}. (a) Two-dimensional PRFI-ZEKE photoelectron spectrum represented as a function of the photoexcitation wavenumber (horizontal axis) and of the square root of the field (vertical axis). The dashed white line was obtained from the experimental data at low fields in a linear regression to determine the position of the field-free ionisation threshold. (b) Two-dimensional PRFI-ZEKE photoelectron spectrum after correction of the field-induced shift of the ionisation threshold. (c) One-dimensional PRFI-ZEKE photoelectron spectra derived by integrating the intensity distributions of the two-dimensional spectrum in Panel (b) between the white horizontal line and the horizontal lines of the corresponding colour. The horizontal dotted white lines represent the value of the prepulse field.

Overall, the PRFI-ZEKE photoelectron spectra in Fig. 8 exhibit the same general qualitative features as the numerical simulations presented in Fig. 7(a)–(c): after correction for the field-induced shifts, the maxima of the intensity distributions

align well with the vertical dashed line in Panel (b); the intensity distributions become asymmetric at high field strengths (compare Panels (b) of Fig. 7 and 8); and the signal strength of the one-dimensional spectra increases but the resolution degrades with increasing width of the integration range.

The comparison of Fig. 8(a)–(c) with Fig. 7(a)–(c) also reveals quantitative differences. (i) In the experimental PRFI-ZEKE photoelectron spectra, no intensity is observed beyond 33 964.75 cm^{-1} and at values of $\sqrt{|F|/(V\,cm^{-1})}$ below 0.4, corresponding to the position of Rydberg states with principal quantum numbers beyond n = 290. In contrast, the calculated spectra extend to $\sqrt{|F|/(V\,cm^{-1})}$ values as low as 0.25, corresponding to a Rydberg-electron binding energy of hc·1.1 cm^{-1} and an n value of 315. It thus appears that, under our experimental conditions, Rydberg states in the n range between 290 and 315 are not detected in the PRFI-ZEKE spectra although the numerical simulations suggest that this should have been the case. (ii) The one-dimensional spectra determined by integration have FWHM that are larger than predicted by the simulations. The narrowest lines have a FWHM of 0.064 cm^{-1} whereas the numerical simulations suggest that significantly narrower lines, down to at least 0.05 cm^{-1}, should have been observed. (iii) The lineshapes of the experimental one-dimensional PRFI-ZEKE photoelectron spectra remain more symmetric as the integration range is increased than predicted by the numerical simulations. These differences suggest that the inversion of the Stark manifolds upon changing the polarity of the electric field after the prepulse is not perfect. The fact that a field-ionisation signal is observed for negative fields with smaller field strength than the prepulse, however, indicates that the Stark-manifold inversion is at least partial. These discrepancies may be caused by stray electric fields in the experimental region and these aspects are discussed further in Section 4.

PRFI-ZEKE photoelectron spectra of the same $(3p)^5\ ^2P_{3/2} \leftarrow (3p)^5(4s)^1\ ^3P_2$ photoionisation transition of Ar, but recorded with a pulse sequence consisting of a prepulse of 0.05 V cm^{-1} followed by a negative-field ramp from −0.03 to −1.10 V cm^{-1}, are displayed in Fig. 9. This second pulse sequence was chosen to observe a broader range of Rydberg states in the PRFI-ZEKE photoelectron spectra. The reduced strength (+0.05 V cm^{-1} instead of +0.21 V cm^{-1}) of the prepulse and the larger range of field strengths covered by the field ramp (negative fields ranging to −1.1 V cm^{-1} instead of −0.34 V cm^{-1}) made it possible to observe both higher (up to $n \approx 375$) and lower Rydberg states (down to $n \approx 145$) and study their field-ionisation dynamics. At n = 150, the spacing between adjacent members of a Rydberg series is more than 2 GHz, so that Rydberg series can easily be resolved.

As expected, the two-dimensional PRFI-ZEKE photoelectron spectrum shown in Fig. 9(a) extends over a broader spectral range than the spectrum in Fig. 8(a), and transitions to individual Rydberg states are visible as vertical stripes in the two-dimensional heat map at wavenumbers below 33 963.2 cm^{-1}. The Rydberg series are resolved up to $n \approx 190$ and are also displayed in the lower panel of Fig. 9(a), which was obtained by integrating the two-dimensional spectrum along the vertical axis. In the range between 33 963.5 and 33 965.5 cm^{-1}, where the Rydberg series are not resolved, the intensity distribution in the two-dimensional spectrum aligns along the dashed white line, indicating that the shift of the ionisation threshold is proportional to $\sqrt{|F|}$. A linear regression yielded a field-free ionisation energy of 33 966.11(10) cm^{-1} and a slope corresponding to c_F = 3.6(3) in eqn (1), in agreement with the results obtained in Fig. 8. The dashed white line does not perfectly describe the field ionisation below 33 964.0 cm^{-1}. In this range, down to approximately 33 962.5 cm^{-1}, the intensity distribution along the $\sqrt{|F|}$ axis broadens and becomes asymmetric. The region of maximal intensity is located below the dashed white line and reveals strong peaks at the positions of individual Rydberg states. Below 33 962.5 cm^{-1}, a second region with significant field-ionisation intensity becomes noticeable, with well-resolved vertical stripes at the positions expected for Rydberg states with n values between 145 and 180. The full white line corresponds to the field-induced shift assuming classical field-ionisation behaviour given by $\Delta E_I/(hc) = -6.12\,cm^{-1}\sqrt{|F|/(V\,cm^{-1})}$. The fact that this second region closely follows the full white line indicates that adiabatic field ionisation becomes important below n = 180 at the electric-field slew rate of 0.2 × 10^6 V cm^{-1} s^{-1} used experimentally. One can therefore conclude that Stark inversion, which requires a diabatic field-ionisation mechanism, cannot be exploited to enhance the resolution of PRFI-ZEKE spectroscopy below n = 180 under our experimental conditions. The range below n = 180 also corresponds to the range where the stray field of about 7.6 mV cm^{-1} in our experiments (see Section 4) is not strong enough to induce substantial ℓ mixing. The Inglis–Teller field, which is the field at which the Stark manifolds of Rydberg states of neighbouring n values start overlapping spectrally,[16] is indeed 9 mV cm^{-1} at n = 180.

Fig. 9(b) displays the same data after correcting for the calculated field-induced shifts. The main part of the intensity distribution is well described by the vertical dashed line corresponding to the field-free ionisation threshold. The resolved Rydberg states, the position of which are not affected by the pulsed field, now appear as diagonal stripes in the figure. A related behaviour was observed by Harper *et al.*[24] in the PRFI-ZEKE photoelectron spectrum of NO and attributed to low-n Rydberg states contributing to the intensity distribution through forced rotational autoionisation. In the present case, the Rydberg-state ionisation mechanism giving rise to the diagonal stripes in Fig. 9(b) is not forced autoionisation but field ionisation, and the effect is observed because the photoexcitation-laser bandwidth and the stray electric field are both small enough that the Rydberg series can be resolved up to high n values. Unlike in Fig. 7(b) and 8(b), the two-dimensional spectrum in Fig. 9(b) does not have any intensity below the dotted line indicating the field strength of the prepulse. The highest observed Rydberg states are located 0.75 cm^{-1} below threshold, corresponding to n values of 380. The 7.6 mV cm^{-1} stray field in our experiment ionises Rydberg states with n values above 530, as discussed in Section 4. One

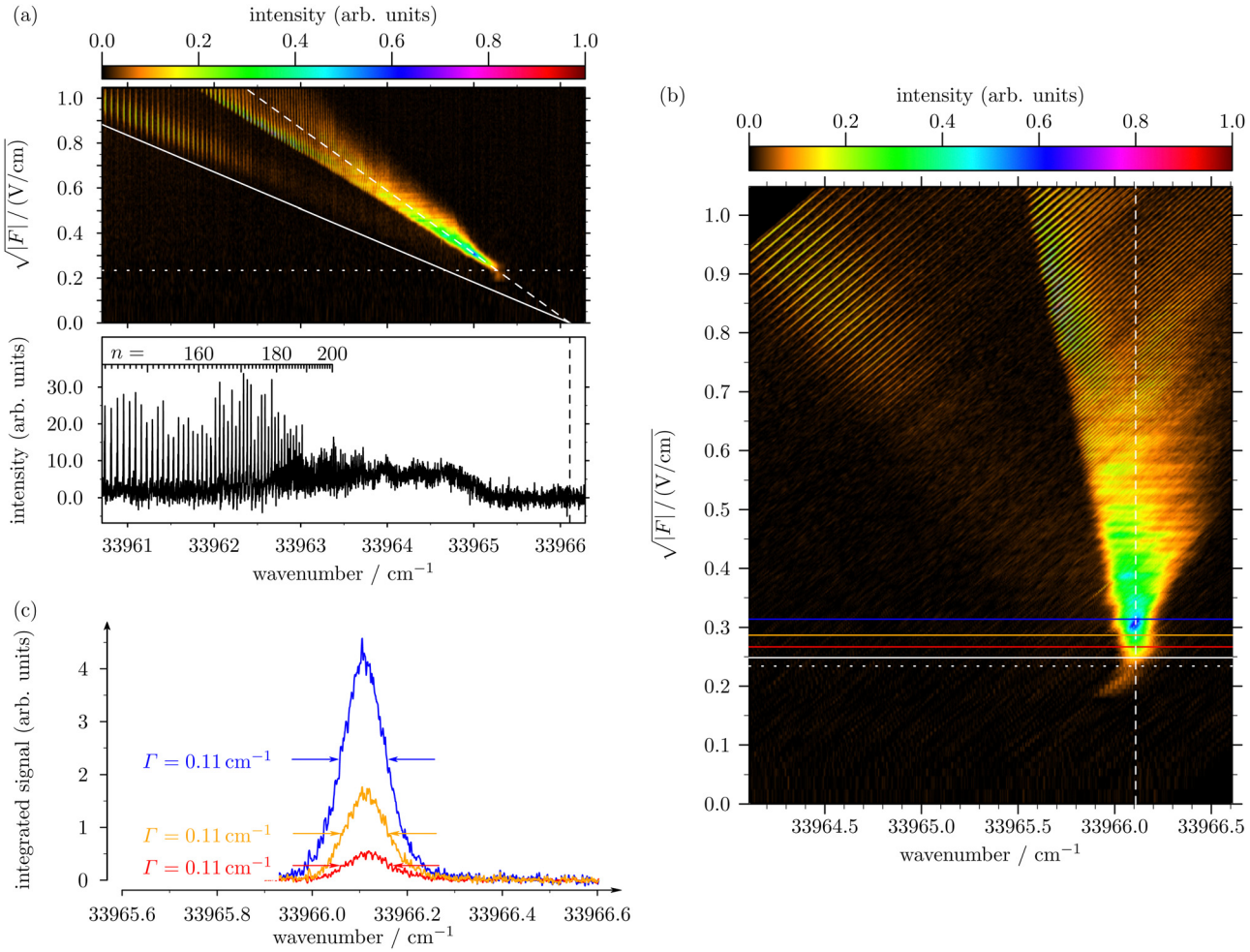

Fig. 9 PRFI-ZEKE photoelectron spectra of the $(3p)^5\,{}^2P_{3/2} \leftarrow (3p)^5(4s)^1\,{}^3P_2$ photoionisation transition of Ar recorded with a pulse sequence consisting of a prepulse of 0.05 V cm^{-1} followed by negative-field ramp from −0.03 to −1.10 V cm^{-1}. (a) Two-dimensional PRFI-ZEKE photoelectron spectrum. The dashed white line was obtained from the experimental data in a linear regression to determine the position of the field-free ionisation threshold. The full white line corresponds to the field-induced shift assuming classical field-ionisation behaviour given by $\Delta E_I/(hc) = -6.12\,\mathrm{cm}^{-1}\sqrt{|F|/(\mathrm{V\,cm}^{-1})}$. The one-dimensional spectrum below the two-dimensional one is obtained by integrating the latter over the complete vertical $\sqrt{F}$ range. Rydberg states up to n = 190 can be resolved. (b) Two-dimensional PRFI-ZEKE photoelectron spectrum after correction of the field-induced shift of the ionisation threshold. (c) One-dimensional PRFI-ZEKE photoelectron spectra derived by integrating the intensity distributions of the two-dimensional spectrum in Panel (b) between the white horizontal line and the horizontal lines of the corresponding colour. The horizontal dotted white lines represent the value of the prepulse field.

can therefore conclude that the Rydberg states in the range between 380 and 530 do not undergo a Stark inversion when the electric field changes polarity before the field ramp, presumably because, under our experimental conditions, the *nkm* Stark states are randomized by stray electric fields.[39] In turn, the spectral resolution of the PRFI-ZEKE photoelectron spectra is not as high as predicted by the numerical simulations. This aspect is illustrated by Fig. 9(c), which displays the one-dimensional PRFI-ZEKE spectra determined by integrating the two dimensional spectrum in Panel (b) between the white horizontal line and the horizontal lines of the corresponding colour. The FWHMs in all three spectra (0.11 cm^{-1}) are thus broader than in Fig. 8(c), where the narrowest line has a full width at half maximum of 0.064 cm^{-1}. This loss of resolution is attributed to the weaker field strength of the prepulse, which restricts the Stark inversion to Rydberg states of higher n values that are more susceptible to stray fields.

One of the important advantages of PRFI-ZEKE photoelectron spectroscopy is that precise values of the field-free ionisation energies can be determined by extrapolation [see dashed white lines in Fig. 8(a) and 9(a)]. Table 1 summarises the field-free ionisation energies of metastable Ar* ($^3P_2$) obtained with pulse sequences differing in the field strengths and the slew rate of the field-ionisation ramp. The uncertainties given in the table are statistical. Systematic uncertainties from the laser-frequency calibration and from Doppler shifts resulting from a deviation from 90° of the angle between laser and supersonic beam are at least an order of magnitude smaller and do not contribute significantly to the overall uncertainty. The results presented in this table are overall consistent with each other

Table 1 Ionisation thresholds ($\tilde{\nu}_{Ar^+\leftarrow Ar^*}$) of metastable Ar corresponding to the Ar^+ ($^2P_{3/2}$) ← $Ar^*(^3P_2)$ ionisation transition as determined from experiments using pulse sequences differing in the values of the field strength (in V cm^{-1}) of the prepulse (F_p) and at the beginning (F_s) and end (F_e) of the field ramp. Γ gives the full width at half maximum of the narrowest lines in the one-dimensional PRFI-ZEKE photoelectron spectra, corresponding to the smallest integration range. The coefficient c_F gives the slope of the linear regression. See text for details

$\lvert F_p\rvert$	$\lvert F_s\rvert$	$\lvert F_e\rvert$	Slewrate / V cm^{-1} s^{-1}	Γ / cm^{-1}	$\tilde{\nu}_{Ar^+\leftarrow Ar^*}$ / cm^{-1}	c_F
0.21	0.07	0.34	0.14×10^6	0.065	33966.07(4)	3.3(4)
0.05	0.03	1.10	0.14×10^6	0.100	33966.11(10)	3.6(4)
0.03	0.03	1.10	0.14×10^6	0.129	33966.18(15)	3.7(4)

and do not reveal strong trends. The ionisation energies agree within the error bars and have a weighted average of 33 966.085(35) cm^{-1}, which is compatible with the more precise value of 33 966.077(5) cm^{-1} [29] one obtains by subtracting the term value of 93 143.7653(30) cm^{-1} of the $Ar^*(^3P_2)$ state from the ionisation energy of Ar (127109.842(4) cm^{-1}). The slopes determining the field-induced shifts obtained from the experimental spectra all correspond to c_F values between 3.2 and 3.7. The widths of the lines in the one-dimensional PRFI-ZEKE spectra corresponding to the narrowest integration range exhibit an increasing trend with decreasing field strength of the prepulse. This effect may be caused by a less complete Stark inversion at the highest n values, which are more sensitive to stray electric fields, as mentioned above and discussed further in Section 4. Considering that Stark inversion is most effective in the field-strength range below the prepulse field strength suggests that ramps covering a wide range of field strengths may be less suitable for the extrapolation. The experimental data obtained with a field ramp extending to −1.1 V cm^{-1} in Fig. 9(a) deviate from a straight line at field strengths beyond 0.3 V cm^{-1} $\left(\sqrt{|F|/(\mathrm{V\,cm^{-1}})} > 0.55\right)$, which introduces a larger uncertainty in the field-free ionisation energies.

3.2 Krypton and Xenon

Similar experiments were also carried out for Kr and Xe, and the results are presented in Fig. 10 and 11. In both figures, Panels (a)–(c) display the PRFI-ZEKE photoelectron spectra recorded with a pulse sequence consisting of a +0.14 mV cm^{-1} prepulse followed by a negative-field ramp starting at the field of −0.05 V cm^{-1} and ending at a field of −0.34 V cm^{-1}, whereas the right panels were obtained using values of +0.07 V cm^{-1}, −0.03 V cm^{-1} and −1.10 V cm^{-1} for these fields, respectively.

The general features of these spectra correspond closely to those observed for Ar. The larger ranges of fields covered by the field ramps used to record the spectra presented on the right side of these figures enabled the observation of resolved Rydberg series in the n range between 145 and 190. The field ionisation of Rydberg states with n values below 180 are observed close to the field expected for adiabatic field ionisation indicated by the full white line, which describes the position of the saddle point in the potential experienced by the electron. Field-ionisation signals are observed at negative fields with weaker strength than the prepulse, indicating that Stark inversion takes place. However, as in Ar, the field range over which the field ionisation is observed is narrower than predicted by the calculations, and the resolution of the one-dimensional PFI-ZEKE photoelectron spectra is only at best 0.075 cm^{-1} in Kr and 0.11 cm^{-1} in Xe. These observations indicate that the inversion of the Stark manifolds upon the polarity reversal of the field between the prepulse and the ramp is not perfect. In the case of Kr, the linewidths are similar to the linewidths observed for the corresponding pulse sequences in Ar. In Xe, the linewidths are significantly broader. Because the isotopic shifts of the ionisation thresholds of Xe are only of the order of 20 MHz per mass unit in Xe,[40] this broadening cannot be attributed to the fact that natural Xe consists of numerous isotopes [^{124}Xe (0.1(1)%); ^{126}Xe (0.09(1)%); ^{128}Xe (1.91(3)%); ^{129}Xe (26.4(6)%); ^{130}Xe (4.1(1)%); ^{131}Xe (21.2(4)%); ^{132}Xe (26.9(5)%); ^{134}Xe (10.4(2)%); ^{136}Xe (8.9(1)%)].[41]

A more likely explanation is that the ionisation signal in Xe was overall stronger than in Kr and that Xe^+ from the discharge could not be deflected from the beam as efficiently, which led to an increase of the background signal in Fig. 11. Consequently, inhomogeneous stray fields from Xe^+ ions in the ionisation volume might have contributed to enhance the randomisation of k and m and thus to degrade the resolution.

Table 2 summarises the ionisation energies of metastable Kr and Xe corresponding to the Rg^+ ($^2P_{3/2}$) ← $Rg^*(^3P_2)$ ionisation thresholds obtained by extrapolation of the PRFI-ZEKE photoelectron spectra to zero field (dashed white lines in Fig. 10(a) and 11(a)). As in the case of Ar, the measurements carried out with field ramps extending to −1.1 V cm^{-1} in Fig. 10(d) and 11(d) reveal deviations of the maximal intensities from a straight line beyond −0.30 V cm^{-1} $\left(\sqrt{|F|/(\mathrm{V\,cm^{-1}})} > 0.55\right)$, which causes a larger uncertainty in the extrapolation to the field-free ionisation thresholds. The weighted averages of these ionisation energies are 32 942.69(4) cm^{-1} for Kr and 30 766.23(4) cm^{-1} for Xe, which in both cases are compatible with the values of 32 942.691(16) cm^{-1} for Kr and 30 766.243(12) cm^{-1} for Xe one obtains by subtracting the term values of the metastable levels from the ground-state ionisation energies using data from the literature.[29]

4 Discussion

The results presented in the previous section indicate that Stark inversion, which is necessary to reach the resolution limit of PRFI-ZEKE photoelectron spectroscopy, is only possible in a narrow range of n values. This range is limited on the low-n side by the onset of adiabatic field ionisation, and on the high-n side by the randomisation of the nkm Stark states induced by (possibly time-dependent) stray fields in the photoexcitation and field-ionisation volume. The pulse sequence used to record the PRFI-ZEKE photoelectron spectra displayed in Fig. 8 appears to be a good compromise to optimise the spectral

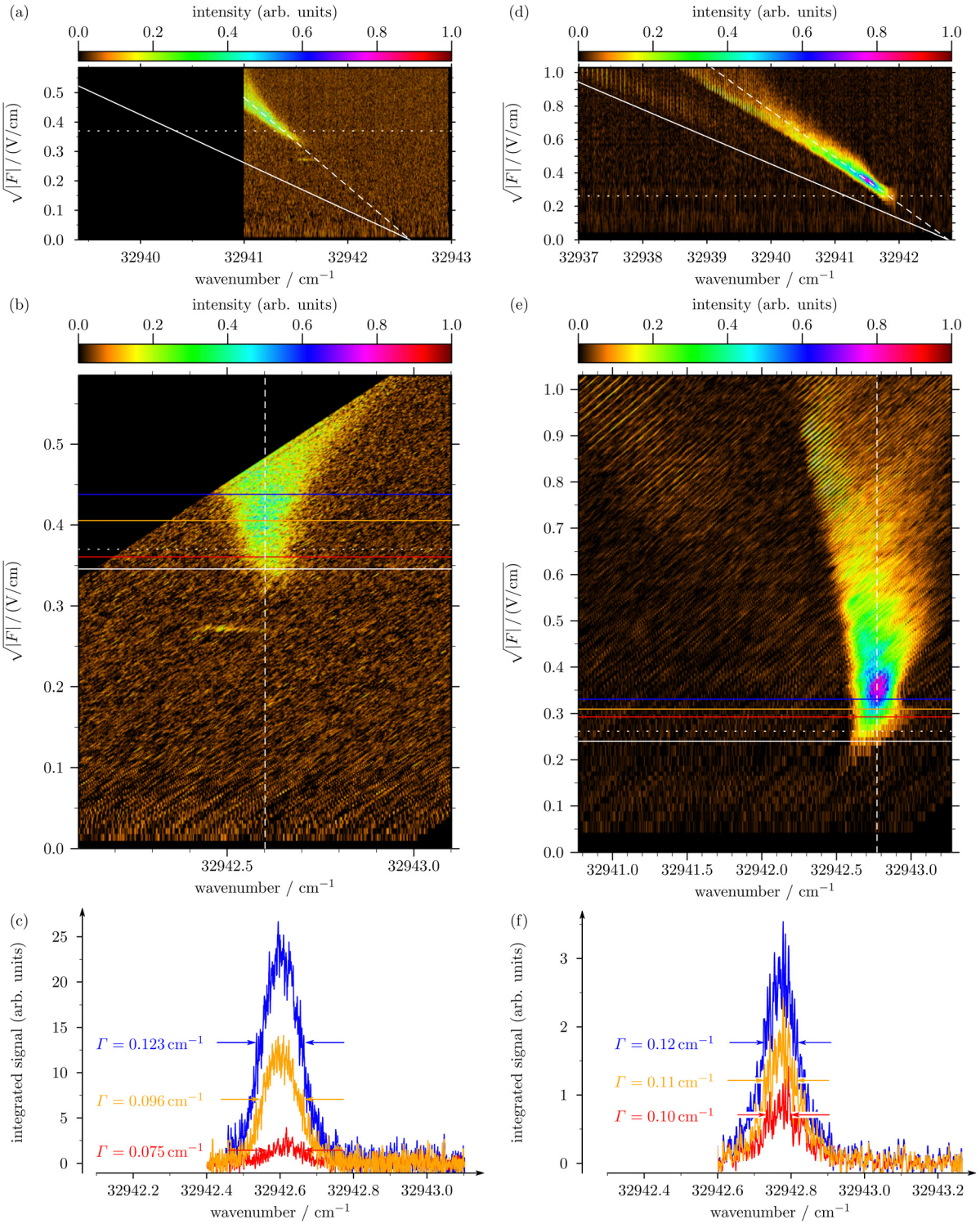

Fig. 10 PRFI-ZEKE photoelectron spectra of the $(4p)^5\,{}^2P_{3/2} \leftarrow (4p)^5(5s)^1\,{}^3P_2$ photoionisation transition of Kr recorded with pulse sequences consisting of a prepulse of 0.14 V cm^{-1} followed by negative-field ramp from −0.05 to −0.34 V cm^{-1} (Panels (a)–(c)) and a prepulse of 0.07 V cm^{-1} followed by negative-field ramp from −0.03 to −1.10 V cm^{-1} (Panels (d)–(f)). Panels (a) and (d): two-dimensional PRFI-ZEKE photoelectron spectra. The dashed white line was obtained from the experimental data in a linear regression to determine the position of the field-free ionisation threshold. The full white line in Panel (d) corresponds to the field-induced shift assuming classical field-ionisation behaviour given by $\Delta E_I/(hc) = -6.12\,\mathrm{cm}^{-1}\sqrt{|F|/(\mathrm{V\,cm}^{-1})}$. Panels (b) and (e): two-dimensional PRFI-ZEKE photoelectron spectra after correction of the field-induced shift of the ionisation threshold. Panels (c) and (f): one-dimensional PRFI-ZEKE photoelectron spectra derived by integrating the intensity distributions of the two-dimensional spectra in Panels (b) and (e) between the white horizontal lines and the horizontal lines of the corresponding colour. The horizontal dotted white lines represent the value of the prepulse field.

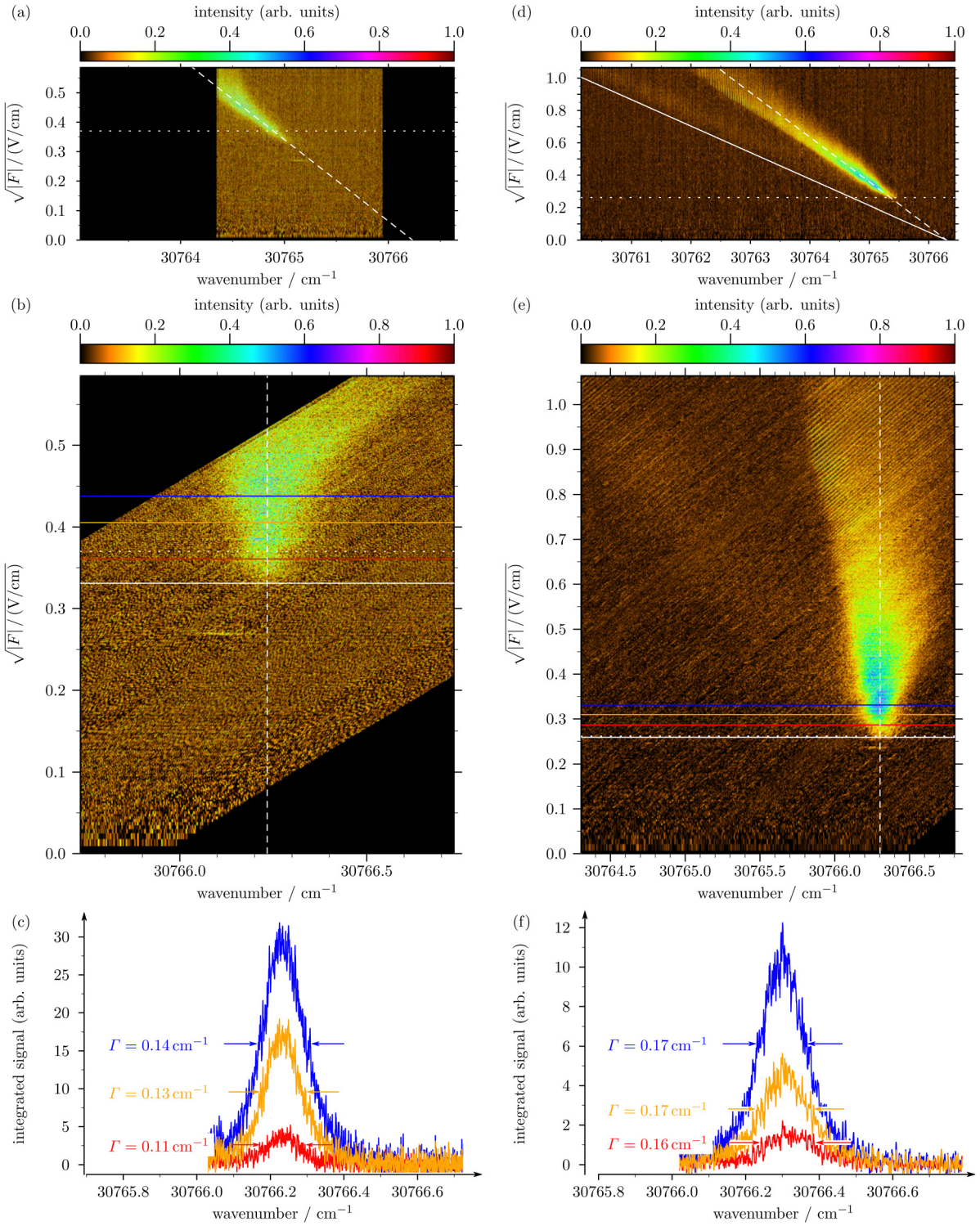

Fig. 11 PRFI-ZEKE photoelectron spectra of the $(5p)^5\,{}^2P_{3/2} \leftarrow (5p)^5(6s)^1\,{}^3P_2$ photoionisation transition of Xe recorded with pulse sequences consisting of a prepulse of 0.14 V cm^{-1} followed by negative-field ramp from −0.05 to −0.34 V cm^{-1} (Panels (a)–(c)) and a prepulse of 0.07 V cm^{-1} followed by negative-field ramp from −0.03 to −1.10 V cm^{-1} (Panels (d)–(f)). Panels (a) and (d): two-dimensional PRFI-ZEKE photoelectron spectrum. The dashed white line was obtained from the experimental data in a linear regression to determine the position of the field-free ionisation threshold. The full white line in Panel (d) corresponds to the field-induced shift assuming classical field-ionisation behaviour given by $\Delta E_1/(hc) = -6.12\,\text{cm}^{-1}\sqrt{|F|/(\text{V cm}^{-1})}$. Panels (b) and (e): two-dimensional PRFI-ZEKE photoelectron spectrum after correction of the field-induced shift of the ionisation threshold. Panels (c) and (f): one-dimensional PRFI-ZEKE photoelectron spectra derived by integrating the intensity distributions of the two-dimensional spectra in Panels (b) and (e) between the white horizontal lines and the horizontal lines of the corresponding colour. The horizontal dotted white lines represent the value of the prepulse field.

Table 2 Ionisation thresholds ($\tilde{\nu}_{Rg^+\leftarrow Rg^*}$) of the metastable rare gas atoms Rg (=Kr and Xe) corresponding to the Rg^+ ($^2P_{3/2}$) ← $Rg^*(^3P_2)$ ionisation transition as determined from experiments using pulse sequences differing in the values of the field strength (in V cm^{-1}) of the prepulse (F_p) and at the beginning (F_s) and end (F_e) of the field ramp. Γ gives the full width at half maximum of the narrowest lines in the one-dimensional PRFI-ZEKE photoelectron spectra, corresponding to the smallest integration range. The coefficient c_F gives the slope of the linear regression. See text for details

$\lvert F_p\rvert$	$\lvert F_s\rvert$	$\lvert F_e\rvert$	Slewrate / V cm^{-1} s^{-1}	Γ / cm^{-1}	$\tilde{\nu}_{Rg^+\leftarrow Rg^*}$ / cm^{-1}	c_F
Kr						
0.14	0.05	0.34	0.14×10^6	0.075	32942.68(4)	3.5(4)
0.07	0.03	1.10	0.14×10^6	0.100	32942.77(10)	3.6(4)
Xe						
0.14	0.05	0.34	0.14×10^6	0.110	30766.22(4)	3.6(4)
0.07	0.03	1.10	0.14×10^6	0.160	30766.31(10)	3.6(4)

resolution in the sense that the range of Rydberg states contributing to the field ionisation signal is located between these two limits. Nevertheless, a more quantitative understanding of the role of stray fields in these experiments is needed to strengthen the argumentation and to find the optimal combination of prepulse and ramp fields to reach a high spectral resolution. One aspect of our measurements that needs to be discussed in this context is the fact that the photoexcitation-laser bandwidth of 30 MHz used to record the spectra would have been sufficient to resolve adjacent members of the Rydberg series beyond n = 550, whereas Rydberg states could only be resolved up to $n \approx 190$ (see Fig. 9).

In this section, we present experiments carried out to measure the stray fields in our experiments and discuss the consequences of these measurements for PRFI-ZEKE spectroscopy. With a laser bandwidth of 30 MHz, the determination of stray electric fields through the measurement of quadratic Stark shifts in high Rydberg states following the procedure described in ref. 38 is not sufficiently accurate. Moreover, the cylindrically symmetric electrode configuration used for field ionisation was optimised to generate homogeneous field distributions in the experimental volume (see Fig. 5). With such an electrode configuration, electric fields can only be controlled along the axis of the electrode stack. Introducing lateral electrodes to control transverse electric fields and compensate stray fields in all three dimensions, as demonstrated in ref. 42, would inevitably degrade the homogeneity of the pulsed-field distributions in the electrode stack. To determine the stray electric fields in our experimental setup, we have therefore followed a different approach and measured the shift of the ionisation thresholds induced by different dc electric fields F_{appl} applied along the axis of the electrode stack. The experiments consisted in measuring the position of the high frequency edge of the delayed pulsed-field-ionisation signal generated by a single pulsed electric field. Electrons emitted in the continuum or with energy higher than the saddle point in the potential consisting of the sum of the Coulomb interaction potential and the $eF_{stray}z$ potential term of the electron-stray-field interaction may escape from the detection region before the field-ionisation pulse is applied.

Fig. 12(a) presents the results obtained at the $(3p)^5\ ^2P_{3/2} \leftarrow (3p)^5(4s)^1\ ^3P_2$ ionisation threshold of Ar. The different spectra displayed in Panel (a) were obtained after applying dc electric fields with strength varying from −34 to 27 mV cm^{-1} along the symmetry axis of the electrode stack. For clarity, the spectra were displaced along the vertical axis by the value of the applied field in mV cm^{-1}. The red lines represent fits of the experimental spectra with a switch function and the dots indicate the positions where the field-ionisation signal reaches half of its maximal value. The spectrum extending furthest to the high-wavenumber side corresponds to the conditions where the dc electric field in the experimental volume is smallest, *i.e.*, where the applied field compensates the stray-field component $F_{stray,z}$ along the symmetry axis of the electrode stack. This situation, corresponding to $F_{comp} = -F_{stray,z}$, is illustrated by the double-headed arrow in Fig. 12(a).

In Fig. 12(b), the half-rise position of the field-ionisation signal is plotted as a function of the z component of the field (F_{appl}) and compared to the values expected from the scaling of the ionisation-threshold shift with the square root of the field.[16,17,43] Based on this scaling, the dependence of the saddle point positions on the applied field can be described by

$$\frac{\tilde{\nu}(F_{appl})}{\text{cm}^{-1}} = \frac{E_I}{hc\,\text{cm}^{-1}} - c_F\left(\frac{(F_{appl}+F_{stray,z})^2+F_{tr}^2}{(\text{V cm}^{-1})^2}\right)^{1/4}, \qquad (2)$$

where $F_{tr} = \sqrt{F_x^2 + F_y^2}$ is the transverse component of the stray field and c_F is a proportionality constant. This constant would be c_F = 6.12 for the classical model for field

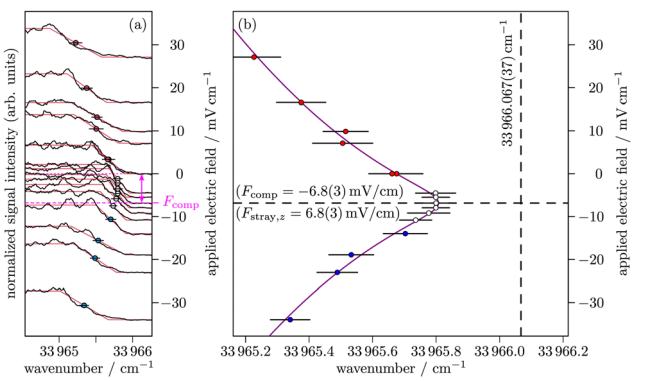

Fig. 12 High-frequency edge of the PFI-ZEKE photoelectron spectrum of the $(3p)^5\ ^2P_{3/2} \leftarrow (3p)^5(4s)^1\ ^3P_2$ photoionisation transition of Ar recorded with a single pulsed field and an intentionally applied dc field of varying strength in the range between −34 mV cm^{-1} and 27 mV cm^{-1}. (a) PFI-ZEKE photoelectron spectra shifted along the vertical axis by the value of the applied dc field in mV cm^{-1}. The red lines are fits of the experimental spectra using a switch function and the dots with error bars mark the half-rise positions. The dashed pink horizontal line indicates the dc electric field F_{comp} needed to compensate the component of the stray electric field along the symmetry axis of the electrode stack (z axis). (b) Dependence of the half-rise positions at the high-frequency edge of the PFI-ZEKE photoelectron spectrum on the applied dc field. The dots with error bars are as in Panel (a). The violet line is the result of a fit based on eqn (2) used to determine the parallel ($F_{stray,z}$) and transverse (F_{tr}) components of the stray field and the field-free ionisation threshold (indicated by the vertical dashed line).

ionisation.[16,17] The violet line in Fig. 12(b) represents the result of a fit to the experimental data, based on eqn (2), of the transverse F_{tr} and parallel $F_{stray,z}$ stray-field components, of the proportionality constant c_F, and of the field-free ionisation threshold E_I. The fit yielded $F_{stray,z}$ = 6.8(3) mV cm^{-1}, F_{tr} = 3.3(8) mV cm^{-1}, c_F = 4.49(3), and $E_I/(hc)$ = 33 966.067(37) cm^{-1}, a value which agrees within the error bars with the value of 33 966.085(35) cm^{-1} determined from the analysis of the PRFI-ZEKE photoelectron spectra (see also Table 1). The value of c_F differs from the value of 6.12 obtained with the classical field-ionisation model. This observation is attributed to the fact that blue-shifted Stark states of high n values located energetically just above the saddle point in the potential have very slow ionisation rates and do not field ionise until the pulsed field is applied. Given the cylindrical symmetry of the electrode stack, the nonzero value of the transverse stray field may indicate that the photoexcitation spot is slightly displaced from the stack axis. Alternatively, it may be caused by ions generated in the experimental volume. Adding $F_{stray,z}$ and F_{tr} in quadrature results in a strength of 7.6 mV cm^{-1} for the stray field.

Such a stray field can affect our experiments through the following effects:

• Firstly, the stray field broadens the transitions to high Rydberg states through the Stark effect. As soon as the full width of the linear Stark manifolds of Rydberg states of neighbouring n values start overlapping – this corresponds to the Inglis–Teller limit[16] – the Rydberg series cannot be resolved spectrally any more. At a field of 7.6 mV cm^{-1}, this situation occurs at $n \approx 190$. With the bandwidth of 30 MHz of the UV laser used in our experiments, Rydberg series could have been resolved up to n values of approximately 625. The Stark effect induced by the stray field thus explains why Rydberg series are not resolved in our experiments beyond n = 190, see, *e.g.*, Fig. 8–12 and, in particular, Panel (a) of Fig. 9.

• Secondly, according to eqn (2) with c_F = 4.49, the stray field prevents the observation of Rydberg states above $n \approx 530$, which have electron binding energies of less than 0.38 cm^{-1}. This effect is not observable in our spectra because the prepulses used in the electric-field pulse sequences were in all cases large enough to field ionise all Rydberg states down to below n = 400 (see Fig. 8–12).

• Thirdly, the transverse components F_{tr} of the stray field can affect the Stark inversion when the applied pulsed electric field crosses the zero-field position between the prepulse and the ramp. At this position, the electric field in the ionisation volume points in the transverse direction, which changes the direction of the quantisation axis and may change the values of k and m.[44] This effect may explain why the linewidths of the experimental one-dimensional PRFI-ZEKE photoelectron spectra are consistently broader than predicted by the numerical simulations. A partial randomisation of k and m would also reduce the field ionisation signal in the range where the field of the ramp is less than the field of the prepulse, and this effect may account for the differences between the numerical and experimental two-dimensional PRFI-ZEKE spectra in Fig. 7(b) and 8(b) below the dotted white line.

• Finally, the width of the Stark manifolds at the highest values of n observed experimentally becomes much larger than the spacing between adjacent members of the Rydberg series. For instance, the highest wavenumbers at which a field-ionisation signal is observed in the PRFI-ZEKE photoelectron spectra displayed in Fig. 8 and 9 are 33 964.8 and 33 965.3 cm^{-1}, respectively, and correspond to n values of approximately 300 and 380, with binding energies of 1.20 and 0.75 cm^{-1}, respectively. The widths of the linear Stark manifolds at n = 300 and n = 380 in a field of 7.6 mV cm^{-1} are 0.09 and 0.14 cm^{-1}, respectively, whereas the spacing between adjacent Rydberg states at these n values are only 0.008 and 0.004 cm^{-1}. Consequently, Rydberg states covering a broad range of n values (of at least 10 around n = 300 and 35 around 380) and k values are simultaneously excited within the laser bandwidth, and this reduces the selectivity of the field-ionisation sequence compared to the situation where the excitation would take place under field-free condition, particularly at the highest n values.

From the results presented in the previous section and the discussion of the effects of stray fields presented above, the following conclusions can be drawn concerning the resolution limit of PRFI-ZEKE photoelectron spectroscopy: (i) to avoid detrimental effects resulting from adiabatic field ionisation, the pulse sequence should ideally field ionise Rydberg states located above the Inglis–Teller limit associated with the stray field (or an intentionally applied field) in the photoexcitation region. For the 7.6 mV cm^{-1} stray field in our experiments, this imposes the condition $n \geq 190$. (ii) Transverse stray fields should be avoided. In the present case, the cylindrical symmetry of the electrode stack naturally limits the strength of the transverse stray field. The compensation of transverse fields using additional electrodes in the transverse plane is in principle possible,[42] but these electrodes tend to be incompatible with the application of spatially homogeneous fields for the field ionisation. In the present case, it was not possible to compensate the 3.3 mV cm^{-1} transverse stray field without sacrificing the homogeneity of the applied fields and the resolution of the PRFI-ZEKE photoelectron spectra. (iii) To avoid the effects of stray fields, which are particularly detrimental at high n values, the field ionisation sequence should not target too high Rydberg states. These criteria imply that a pulse sequence designed for the field ionisation of Rydberg states with n in the range between approximately 200 and 250, with binding energies in the range between 2.7 and 1.7 cm^{-1} below the field-free threshold, is best suited to reach high resolution in PRFI-ZEKE photoelectron spectra in our experimental setup. Numerical simulations such as those presented in Subsection 2.2 indicate that a prepulse of about 0.4 V cm^{-1} is ideal for this purpose.

Fig. 13 presents PRFI-ZEKE photoelectron spectra of the $(3p)^5\ ^2P_{3/2} \leftarrow (3p)^5(4s)^1\ ^3P_2$ photoionisation transition of Ar recorded with a 0.41 V cm^{-1} prepulse followed by a ramped field starting at −0.14 V cm^{-1} and ending at −0.68 V cm^{-1} with a slew rate of 0.55 × 10^6 V cm^{-1} s^{-1}. As in Fig. 8–11, the figure presents the two-dimensional PRFI-ZEKE-photoelectron

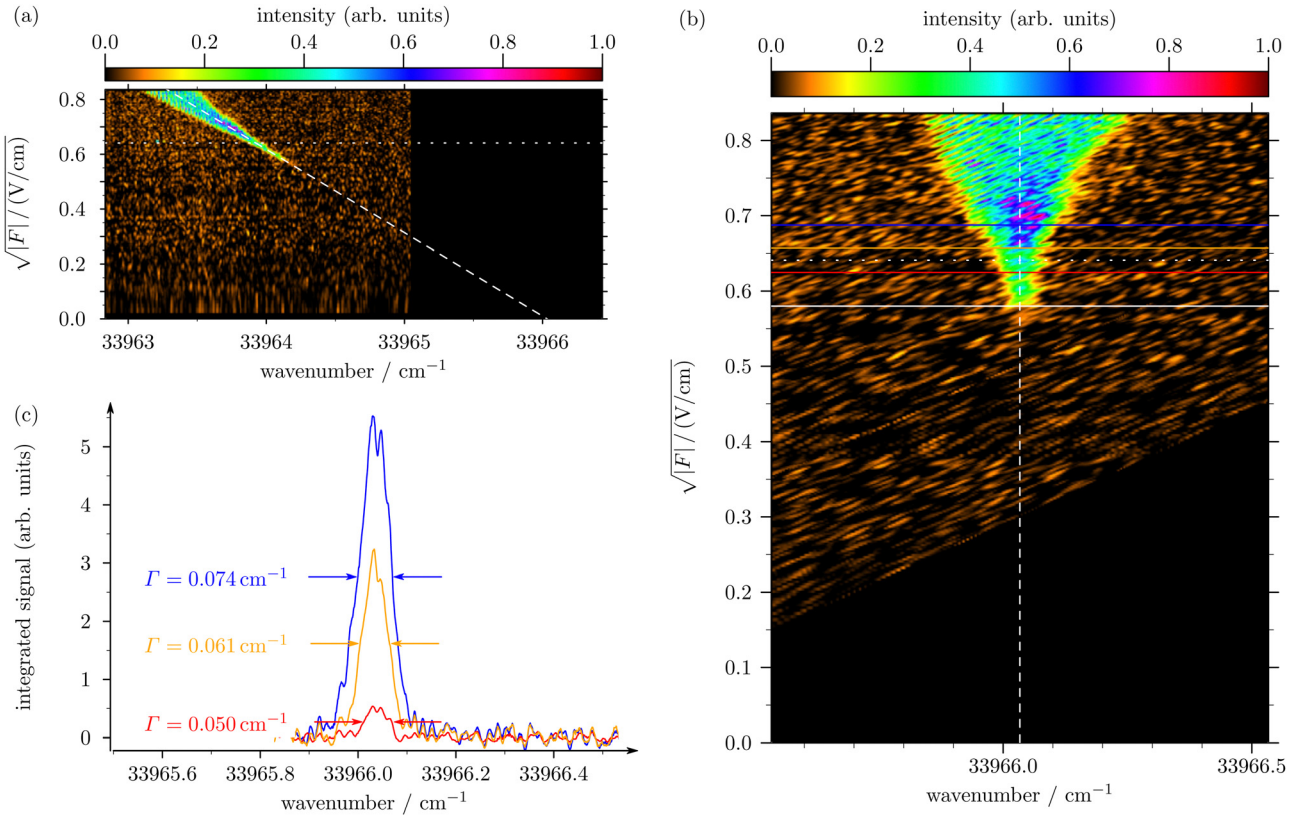

Fig. 13 PRFI-ZEKE photoelectron spectra of the $(3p)^5\ ^2P_{3/2} \leftarrow (3p)^5(4s)^1\ ^3P_2$ photoionisation transition of Ar recorded with a pulse sequence consisting of a prepulse of 0.41 V cm^{-1} followed by a negative-field ramp from −0.14 to −0.68 V cm^{-1}. (a) Two-dimensional PRFI-ZEKE photoelectron spectrum. The dashed white line was obtained from the experimental data in a linear regression to determine the position of the field-free ionisation threshold. (b) Two-dimensional PRFI-ZEKE photoelectron spectrum after correction of the field-induced shift of the ionisation threshold. (c) One-dimensional PRFI-ZEKE photoelectron spectra derived by integrating the intensity distributions of the two-dimensional spectrum in Panel (b) between the white horizontal line and the horizontal lines of the corresponding colour. The horizontal dotted white lines represent the value of the prepulse field.

spectra before and after correcting the field-induced shifts in Panels (a) and (b), respectively, and the one-dimensional PRFI-ZEKE-photoelectron spectra corresponding to the colour-labelled integration ranges in Panel (c). Compared to the results presented in Fig. 8(c), the resolution is improved by about 20% and the narrowest line has a FWHM of only 0.05 cm^{-1}, which is unprecedented in photoelectron spectroscopy. The value of the field-free ionisation threshold derived from this measurement, 33966.03(3) cm^{-1}, agrees with the values determined in the other measurements presented in Section 3 within the error bars.

5 Conclusion and outlook

This article has presented the results of an investigation of the resolution limit of PRFI-ZEKE photoelectron spectroscopy, which is an improved variant of PFI-ZEKE photoelectron spectroscopy recently introduced by Harper *et al.*[24] As in earlier work by Dietrich *et al.*[5] and Hollenstein *et al.*,[6] this method exploits the enhanced selectivity in the diabatic field ionisation of high Rydberg states that results from a pulse sequence during which the polarity of the electric field is inverted after a prepulse. Instead of the sequence of staircase pulses used in ref. 6, the pulse sequence used by Harper *et al.* relies on a slowly rising electric-field ramp, which leads to the recording of two-dimensional spectra that consist of electron time-of-flight spectra at all laser-excitation wavenumbers. PRFI-ZEKE photoelectron spectroscopy brings the following important advantages. (i) The resolution is no longer limited by the finite size of the field steps in the staircase pulse; (ii) the two-dimensional spectra contain a full map of the field-ionisation dynamics of a broad range of Rydberg states and enable one to distinguish between contributions from autoionisation and field ionisation; (iii) the two-dimensional spectra can be analysed after the measurements to search for regions yielding photoelectron spectra with optimal spectral resolution or to search for the best compromise between resolution and signal-to-noise ratio. The only disadvantage compared to PFI-ZEKE photoelectron spectroscopy is the much higher data-memory capacity required to save the entire electron-TOF spectra instead of just a single integrated value per step in the staircase pulse sequence. For example, at a sampling rate of 500 Msample s^{-1}, the data size for a single 3 cm^{-1} – long wavenumber scan with a step size of 0.001 cm^{-1} and a TOF-sample span of 1 μs (sample size 500) is in the range of 200–300 MB compared to

Table 3 Ionisation energies E_I of the metastable rare-gas atoms Rg (=Ar, Kr and Xe) corresponding to the Rg^+ ($^2P_{3/2}$) ← Rg*($^3P_2$) ionisation thresholds as determined from PRFI-ZEKE photoelectron spectra. The values are compared to the differences between the ground-state ionisation energies and their uncertainties from ref. 29 and the term values of the $^3P_2$ metastable states of the rare-gas atoms with the uncertainties taken from the original literature, ref. 45–47 for Ar, ref. 45 and 48–50 for Kr, and ref. 45, 51 and 52 for Xe

Rg	$[E_{I,exp.}/(hc)]/cm^{-1}$	$[E_{I,lit.}/(hc)]/cm^{-1}$	$\Delta_{exp\text{-}lit}/cm^{-1}$
Ar	33 966.08(4)	33 966.077(5)	0.003(40)
Kr	32 942.69(4)	32 942.691(16)	−0.002(40)
Xe	30 766.23(4)	30 766.243(12)	0.013(40)

~10 kB in conventional PFI-ZEKE PES. However, in the big-data era, neither the storage nor the processing of data sets of these sizes represent significant problems.

In a series of measurements carried with different prepulse field strengths and different field ramps, we determined the field-free ionisation energies of the metastable rare gas atoms Rg* $(np)^5((n+1)s)^1\ ^3P_2$, with n = 3, 4 and 5 for Ar, Kr and Xe, as summarised in Table 3. The accuracy of about 0.04 cm^{-1} of these results is limited by the extrapolation to the field-free thresholds. These ionisation energies are in good agreement with the values one can determine from reference data[29] on the ground-state ionisation energies and the term values of the metastable states.

When analysing the factors influencing the resolution, such as the field strength of the prepulse and the presence of longitudinal and transverse stray-field components, we observed that the Rydberg states of all three atoms follow an adiabatic ionisation mechanism below $n \approx 190$, which corresponds to the Inglis–Teller limit for the value of 7.6 mV cm^{-1} of the stray field present in the experimental volume. We also observed that the Rydberg states for which the Stark inversion is least perturbed by stray fields under our experimental conditions are located just above the Inglis–Teller limit. The contributions from these states to the PRFI-ZEKE photoelectron spectra could be optimised by using a prepulse of 0.4 V cm^{-1}. With such a prepulse, we could improve the resolution of the PRFI-ZEKE photoelectron spectrum of Ar to 0.05 cm^{-1}, which is unprecedented in photoelectron spectroscopy. We expect that this resolution can be improved further by a better control of the stray fields.

Conflicts of interest

There are no conflicts to declare.

Acknowledgements

We thank Dr Raphaël Hahn for his help with the SIMION simulation and Hansjürg Schmutz and Josef A. Agner for technical support. This work was supported financially by the Swiss National Science Foundation (Grant No. 200020B-200478).

References

1 G. Reiser, W. Habenicht, K. Müller-Dethlefs and E. W. Schlag, *Chem. Phys. Lett.*, 1988, **152**, 119–123.
2 K. Müller-Dethlefs and E. W. Schlag, *Ann. Rev. Phys. Chem.*, 1991, **42**, 109–136.
3 K. Müller-Dethlefs and E. W. Schlag, *Angew. Chem.*, 1998, **37**, 1346–1374.
4 F. Merkt, S. Willitsch and U. Hollenstein, in *Handbook of High-Resolution Spectroscopy*, ed. M. Quack and F. Merkt, John Wiley & Sons, Chichester, 2011, vol. 3, pp. 1617–1654.
5 H.-J. Dietrich, K. Müller-Dethlefs and L. Y. Baranov, *Phys. Rev. Lett.*, 1996, **76**, 3530–3533.
6 U. Hollenstein, R. Seiler, H. Schmutz, M. Andrist and F. Merkt, *J. Chem. Phys.*, 2001, **115**, 5461–5469.
7 V. Goncharov, L. A. Kaledin and M. C. Heaven, *J. Chem. Phys.*, 2006, **125**, 133202.
8 B. J. Barker, I. O. Antonov and M. C. Heaven, *J. Mol. Spectrosc.*, 2012, **275**, 35–40.
9 Z. Luo, Y.-C. Chang, H. Huang and C. Y. Ng, *J. Phys. Chem. A*, 2015, **119**, 11162–11169.
10 Z. Luo, Y.-C. Chang, Y. Pan, K.-C. Lau and C. Y. Ng, *J. Phys. Chem. A*, 2016, **120**, 4643–4654.
11 R. Lindner, K. Müller-Dethlefs, E. Wedum, K. Haber and E. R. Grant, *Science*, 1996, **271**, 1698–1702.
12 S. Willitsch, U. Hollenstein and F. Merkt, *J. Chem. Phys.*, 2004, **120**, 1761–1774.
13 H. J. Wörner and F. Merkt, *J. Chem. Phys.*, 2007, **127**, 034303.
14 A. M. Schulenburg and F. Merkt, *J. Chem. Phys.*, 2009, **130**, 034308.
15 K. Vasilatou, J. M. Michaud, D. Baykusheva, G. Grassi and F. Merkt, *J. Chem. Phys.*, 2014, **141**, 064317.
16 T. F. Gallagher, *Rydberg Atoms*, Cambridge University Press, Cambridge, 1994.
17 W. A. Chupka, *J. Chem. Phys.*, 1993, **98**, 4520–4530.
18 H. A. Bethe and E. E. Salpeter, *Quantum Mechanics of One- and Two-Electron Atoms*, Springer, Berlin, 1957.
19 R. J. Damburg and V. V. Kolosov, *J. Phys. B: At. Mol. Phys.*, 1979, **12**, 2637–2643.
20 S. Mollet and F. Merkt, *J. Chem. Phys.*, 2013, **139**, 034302.
21 B. Gans, G. Grassi and F. Merkt, *J. Phys. Chem.*, 2013, **117**, 9353–9362.
22 U. Hollenstein, K. Dulitz and F. Merkt, *Mol. Phys.*, 2019, **117**, 2956–2960.
23 H. Herburger, U. Hollenstein, J. A. Agner and F. Merkt, *J. Chem. Phys.*, 2019, **151**, 144302.
24 O. J. Harper, N. L. Chen, S. Boyé-Péronne and B. Gans, *Phys. Chem. Chem. Phys.*, 2022, **24**, 2777–2784.
25 A. Deller, M. H. Rayment and S. D. Hogan, *Phys. Rev. Lett.*, 2020, **125**, 073201.
26 A. Osterwalder, M. J. Nee, J. Zhou and D. M. Neumark, *J. Chem. Phys.*, 2004, **121**, 6317–6322.
27 J. C. Poully, J. P. Schermann, N. Nieuwjaer, F. Lecomte, G. Grégoire, C. Desfrançois, G. A. Garcia, L. Nahon,

D. Nandi, L. Poisson and M. Hochlaf, *Phys. Chem. Chem. Phys.*, 2010, **12**, 3566–3572.
28 Z. Lu, H. Gao, Y.-T. Xu, L. Yang, C.-S. Lam, Y. Benitez and C. Y. Ng, *Chin. J. Chem. Phys.*, 2016, **29**, 59–69.
29 V. L. Sukhorukov, I. D. Petrov, M. Schäfer, F. Merkt, M.-W. Ruf and H. Hotop, *J. Phys. B: At., Mol. Opt. Phys.*, 2012, **45**, 092001.
30 H. Herburger, J. A. Agner, H. Schmutz, U. Hollenstein and F. Merkt, 2023, unpublished results.
31 A. Gerakis, M. N. Shneider and B. C. Stratton, *Appl. Phys. Lett.*, 2016, **109**, 031112.
32 A. Gerakis, M. N. Shneider, Y. Raitses and B. C. Stratton, *Optical Trapping and Optical Micromanipulation XIV*, 2017, p. 103470J.
33 A. Gerakis, *Controlling and probing molecular motion with optical lattices*, PhD thesis, University College London, London, United Kingdom, 2014.
34 T. W. Hänsch, I. S. Shahin and A. L. Schawlow, *Phys. Rev. Lett.*, 1971, **27**, 707–710.
35 Designed by S. Leutwyler and H. M. Frey, Constructed by the mechanical and electronic workshops of the Department of Chemistry and Biochemistry, Freiestrasse 3, Universität Bern, CH-3012 Bern, Switzerland, 2014.
36 D. Manura and D. A. Dahl, *SIMION 3D, version 8.0 user's manual*, Scientific Instrument Services, Inc., Ringoes, New Jersey, USA, 2007.
37 H.-J. Dietrich, R. Lindner and K. Müller-Dethlefs, *J. Chem. Phys.*, 1994, **101**, 3399–3402.
38 A. Osterwalder and F. Merkt, *Phys. Rev. Lett.*, 1999, **82**, 1831–1834.
39 F. Merkt, *J. Chem. Phys.*, 1994, **100**, 2623–2628.
40 H. Herburger, E. Toutoudaki, U. Hollenstein and F. Merkt, 2023, unpublished results.
41 I. Mills, T. Cvitaš, K. Homann, N. Kallay and K. Kuchitsu, *Quantities, Units and Symbols in Physical Chemistry*, Blackwell Science, Oxford, 2nd edn, 1993.
42 N. Hölsch, M. Beyer, E. J. Salumbides, K. S. E. Eikema, W. Ubachs, Ch Jungen and F. Merkt, *Phys. Rev. Lett.*, 2019, **122**, 103002.
43 F. Merkt, *Ann. Rev. Phys. Chem.*, 1997, **48**, 675–709.
44 H. Palm and F. Merkt, *Chem. Phys. Lett.*, 1997, **270**, 1–8.
45 J. E. Sansonetti and W. C. Martin, *J. Phys. Chem. Ref. Data*, 2005, **34**, 1559–2259.
46 I. Velchev, W. Hogervorst and W. Ubachs, *J. Phys. B: At., Mol. Opt. Phys.*, 1999, **32**, L511–L516.
47 L. Minnhagen, *J. Opt. Soc. Am.*, 1973, **63**, 1185–1198.
48 S. Galtier, R. K. Altmann, L. S. Dreissen and K. S. E. Eikema, *Appl. Phys. B*, 2017, **123**, 1–10.
49 F. Brandi, W. Hogervorst and W. Ubachs, *J. Phys. B: At., Mol. Opt. Phys.*, 2002, **35**, 1071–1084.
50 V. Kaufman, *J. Res. Natl. Inst. Stand. Technol.*, 1993, **98**, 717–724.
51 F. Brandi, I. Velchev, W. Hogervorst and W. Ubachs, *Phys. Rev. A: At., Mol., Opt. Phys.*, 2001, **64**, 032505.
52 C. J. Humphreys and E. Paul, Jr., *J. Opt. Soc. Am.*, 1970, **60**, 1302–1310.

